Article

Recurrent *UBE3C-LRP5* translocations in head and neck cancer with therapeutic implications

Check for updates

Bhasker Dharavath [1,2], Ashwin Butle[1,3], Akshita Chaudhary[1], Ankita Pal[1], Sanket Desai[1], Aniket Chowdhury[1,2], Rahul Thorat[4], Pawan Upadhyay [1], Sudhir Nair[2,5] & Amit Dutt [1,2,6] ✉

Head and neck cancer is a major cause of morbidity and mortality worldwide. The identification of genetic alterations in head and neck cancer may improve diagnosis and treatment outcomes. In this study, we report the identification and functional characterization of *UBE3C-LRP5* translocation in head and neck cancer. Our whole transcriptome sequencing and RT-PCR analysis of 151 head and neck cancer tumor samples identified the *LRP5-UBE3C* and *UBE3C-LRP5* fusion transcripts in 5.3% of patients of Indian origin ($n = 151$), and *UBE3C-LRP5* fusion transcripts in 1.2% of TCGA-HNSC patients ($n = 502$). Further, whole genome sequencing identified the breakpoint of *UBE3C-LRP5* translocation. We demonstrate that *UBE3C-LRP5* fusion is activating in vitro and in vivo, and promotes the proliferation, migration, and invasion of head and neck cancer cells. In contrast, depletion of *UBE3C-LRP5* fusion suppresses the clonogenic, migratory, and invasive potential of the cells. The *UBE3C-LRP5* fusion activates the Wnt/β-catenin signaling by promoting nuclear accumulation of β-catenin, leading to upregulation of Wnt/β-catenin target genes, *MYC, CCND1, TCF4*, and *LEF1*. Consistently, treatment with the FDA-approved drug, pyrvinium pamoate, significantly reduced the transforming ability of cells expressing the fusion protein and improved survival in mice bearing tumors of fusion-overexpressing cells. Interestingly, fusion-expressing cells upon knockdown of *CTNNB1*, or *LEF1* show reduced proliferation, clonogenic abilities, and reduced sensitivity to pyrvinium pamoate. Overall, our study suggests that the UBE3C-LRP5 fusion is a promising therapeutic target for head and neck cancer and that pyrvinium pamoate may be a potential drug candidate for treating head and neck cancer harboring this translocation.

Gene fusion is caused by chromosomal rearrangements or aberrant splicing mechanisms[1,2]. They frequently affect genes that play a role in oncogenesis, such as tyrosine kinases, chromatin regulators, and transcription factors[1]. Although fusion transcripts are challenging to identify, their presence in cancer cells often indicates a greater degree of oncogenic dependency, making them attractive therapeutic targets[3]. The US Food and Drug Administration granted Breakthrough Therapy Designation to several

agents targeting the fusion protein and approved them for the treatment of solid tumors harboring fusion genes such as *NTRK, ALK, RET, ROS1, BRAF,* and *RAF1*, among others. Larotrectinib and entrectinib, for instance, target NTRK fusions, selpercatinib targets RET fusions, and dabrafenib and trametinib target BRAF fusions[4–11]. The significance of identifying and targeting gene fusions in the treatment of solid tumors has been highlighted by these tumor-independent therapies. The discovery of oncogenic gene

[1]Integrated Cancer Genomics Laboratory, Advanced Centre for Treatment, Research, and Education in Cancer, Kharghar, Navi Mumbai, Maharashtra 410210, India. [2]Homi Bhabha National Institute, Training School Complex, Anushakti Nagar, Mumbai, Maharashtra 400094, India. [3] Department of Biochemistry, All India Institute of Medical Sciences, Nagpur, Maharashtra 441108, India. [4]Laboratory Animal Facility, Advanced Centre for Treatment, Research and Education in Cancer, Kharghar, Navi Mumbai, Maharashtra 410210, India. [5]Division of Head and Neck Oncology, Department of Surgical Oncology, Tata Memorial Hospital, Tata Memorial Centre, Parel, Mumbai 400012, India. [6]Present address: Department of Genetics, University of Delhi South Campus, New Delhi 110021, India. ✉e-mail: adutt@actrec.gov.in; amitdutt@south.du.ac.in

THE HORMEL INSTITUTE
UNIVERSITY OF MINNESOTA

1

fusions has led to the development of tissue-agnostic treatment strategies that have increased cancer patient survival[12].

Among solid tumors, head and neck squamous cell carcinoma (HNSCC) is one of the most common cancers in developing countries and the sixth most common cancer worldwide[13,14]. Despite the high burden of genomic aberrations in HNSCC, the landscape of fusion genes remains largely unexplored[15]. The identification of therapeutically relevant fusion genes in HNSCC could help in the development of targeted therapies for patients regardless of the tumor subsite. There are few reports on fusion genes in HNSCC, such as *FGFR3-TACC3* fusion[2] and *MYB-NFIB* fusion. In vitro studies have shown that *FGFR3-TACC3* fusion[16] could play a role in resistance to *EGFR/ERBB3* inhibition in HNSCC[17]. There are other reports on gene fusions in HNSCC samples[18,19] and cell lines[20], but they lack clinical data, and no drugs have been approved against fusion genes as targeted therapies for head and neck cancer. Therefore, identifying and characterizing therapeutically relevant fusion transcripts in HNSCC could help to develop targeted therapies for this cancer.

In this study, we identified a recurrent, and therapeutically relevant inter-chromosomal fusion, *UBE3C-LRP5*, through transcriptome sequencing and RT-PCR-based analysis of HNSCC primary tumor samples. The fusion transcript constitutively activates the Wnt/β-catenin pathway, which promotes proliferation, migration, and invasion of HNSCC cell lines. The fusion was found to be transforming in vitro and in vivo, and responded to an FDA-approved anthelminthic drug, pyrvinium pamoate. Targeting the fusion protein with pyrvinium pamoate represents a potential therapeutic approach for managing patients with head and neck cancer. The identification and characterization of *UBE3C-LRP5* translocation in HNSCC could provide new insights into the biology of the disease and aid in the development of targeted therapies for patients with this cancer.

Results
Identification and validation of *LRP5-UBE3C* and *UBE3C-LRP5* translocations in head and neck cancer

We performed whole transcriptome sequencing of five adjacent normal, ten head and neck tumor samples, and four head and neck cancer cell lines (Supplementary Fig. S1) to generate an average of 25 and 34 million paired-end reads, respectively. Using Chimerascan, we performed fusion analysis and identified a total of 242 unique somatic fusion transcripts (Supplementary Figs. S2a, b, S3a–d and Supplementary Table S6). We compared our data with fusion databases (detailed in Materials and Methods) and observed 47 unique transcript fusions overlap, showing identical fusion transcript pairs (Supplementary Table S7).

Among 242 potential fusion transcripts, 12 high-confidence fusion transcripts, including five previously unreported fusion transcripts, were selected for validation using Sanger sequencing based on the following criteria: the presence of an appropriate donor (5') and acceptor (3') relationship, the presence of reads spanning the junction region, and those recurrent across multiple samples or expressed at a very high level (Supplementary Table S8). This validation process was performed across the first validation set comprising 44 primary head and neck tumors, which notably included the ten tumors previously subjected to transcriptome sequencing (Supplementary Figs. S1, S4 and Supplementary Table S9), alongside four head and neck cancer cell lines. *CLN6-CALML4* (9/48), *LRP5-UBE3C* (7/48), *RRM2-C2orf48* (7/48), *YIF1A-RCOR2* (6/48), *POLA2-CDC42EP2* (4/48), *SLC39A1-CRTC2* (2/48), *BACH1-GRIK1* (2/48), *EXT1-MED30* (2/48), fusions transcripts were found to be recurrent, whereas *NAIP-GTF2H2B*, *PSMD5-VAV2*, *CTSC-RAB38*, and *FTSJD2-BTBD9* fusion transcripts were observed as non-recurrent (Supplementary Fig. S5a, b). We further prioritized the potential somatic fusion transcripts for functional characterization based on the following criteria: recurrence in patient samples; presence in at least one cell line, which can serve as a model system for genetic perturbation experiments; not reported previously in any fusion databases or literature; and, one of the gene partners in the fusion transcript is reported to play an important role in cancer. Based on these criteria, we prioritized the *LRP5-UBE3C* fusion transcript for functional characterization in head and neck

cancer. *LRP5* is a transmembrane low-density lipoprotein receptor involved in the Wnt/β-catenin signaling pathway[21], and *UBE3C* is an E3 ubiquitin ligase that transfers ubiquitin from the E2 ubiquitin-conjugating enzyme to the substrate[22].

LRP5-UBE3C is an inter-chromosomal fusion transcript of *LRP5* on chromosome 11q13.2 and *UBE3C* on chromosome 7q36.3 in the NT-8e cell line and six of head and neck cancer patients. In the transcriptome sequencing data of the NT-8e cell line, we identified two variants of the *LRP5-UBE3C* fusion transcript, *LRP5-UBE3C* (v1) and *LRP5-UBE3C* (v2) (Supplementary Fig. S6a–e). The fusion transcript variants were validated by RT-PCR and Sanger sequencing in the NT-8e cell line cDNA (Supplementary Fig. S7a–c). In the six patient samples, only one *LRP5-UBE3C* (v1) variant was detected (Supplementary Fig. S8a, b).

Next, we investigated whether *LRP5* and *UBE3C* fuse at the genomic DNA level to form *LRP5-UBE3C* fusion transcript variants. To identify the translocation breakpoint, we performed whole genome sequencing of the NT-8e cell line (Supplementary Fig. S1) to generate 800 million raw reads, with 35X coverage and analyzed the translocation breakpoint using SvABA and MANTA structural variant analysis tools. Interestingly, we found a unique contig of 400 bp mapping to *LRP5* and *UBE3C* genes. Mapping the junction and spanning reads to the human genome suggested that the translocation breakpoint is located in intron 22 of *UBE3C* and intron 5 of *LRP5* at the genomic DNA level (Fig. 1a). It is noteworthy to mention that of the 10.5 kb intron 22 of *UBE3C*, only 761 bases were retained, and of the 20 kb intron 5 of *LRP5*, only 2.3 kb was retained in the fusion gene at the genomic DNA level. Surprisingly, the *UBE3C* part of the fusion was found to be an inverted 5'-partner gene, suggesting a new fusion variant, *UBE3C-LRP5* (Fig. 1b). To validate the *UBE3C-LRP5* translocation breakpoint and its directionality at the genomic DNA level, orthologous techniques, PCR, and Sanger sequencing were used. PCR and Sanger sequencing analyses confirmed the *UBE3C-LRP5* translocation breakpoint and inversion of the *UBE3C* part at the genomic DNA level (Supplementary Fig. S9a–c).

Further, we investigated whether the *UBE3C-LRP5* translocation transcribed a fusion transcript. Of note, we missed to find spanning/junction reads supporting this fusion in the transcriptome sequencing data of the NT-8e cell line, potentially attributable to the limited coverage of 28 million paired-end reads. We designed primers and performed RT-PCR to identify the *UBE3C-LRP5* fusion transcript in the cDNA of NT-8e cells. Surprisingly, RT-PCR-based amplification of the *UBE3C-LRP5* fusion transcript displayed two distinct bands on agarose gel (Supplementary Fig. S10a). Sanger sequencing of the bands identified two variants of *UBE3C-LRP5* fusion (*UBE3C-LRP5* (v1) and *UBE3C-LRP5* (v2)) in the NT-8e cell line (Supplementary Fig. S10b, c). The *UBE3C-LRP5* (v1) variant is a fusion of inverted exon 23 of *UBE3C*, with 12 bp of retained intron 5 of *LRP5* and exon 6–23 of *LRP5*. The *UBE3C-LRP5* (v2) variant is a fusion of inverted exon 23 of *UBE3C* and exon 6–23 of *LRP5* with a deletion of 188 bases from the start of exon 6 of *LRP5*. To examine the presence of both *LRP5-UBE3C* (v1, v2), and *UBE3C-LRP5* (v1, v2) fusion variants, we performed RT-PCR analysis on the cDNA from a total of 151 head and neck tumor samples. This set included the 44 tumor samples from the first validation set (Supplementary Figs. S1, S4 and Supplementary Table S9). We identified *LRP5-UBE3C* (v1) fusion in 4% (6/151) and *UBE3C-LRP5* (v2) fusion in 2.6% of (4/151) head and neck cancer patients (Supplementary Figs. S8a, b, S11a, b). Importantly, we also validated the UBE3C-LRP5 fusion protein in the NT-8e cell line using western blotting (Supplementary Fig. S12). Unfortunately, we were unable to conduct similar validation for primary tumors derived from tongue cancer patients due to the limited availability of samples.

To explore whether the fusion is present in head and neck cancer patients of Caucasian origin, we analyzed TCGA-HNSC transcriptome sequencing data (*n* = 502) (Supplementary Fig. S1). Interestingly, we found six different *UBE3C-LRP5* fusion transcript variants (v3–v8) in six (6/502) TCGA-HNSC patient samples (1.2%). Importantly, all predicted UBE3C-LRP5 fusion proteins (v1–v8) retain the functional cytoplasmic domain of LRP5 (Fig. 1c, d). As the *UBE3C* gene is inverted in the *UBE3C-LRP5* fusion, the protein domains of UBE3C are not present in the fusion protein
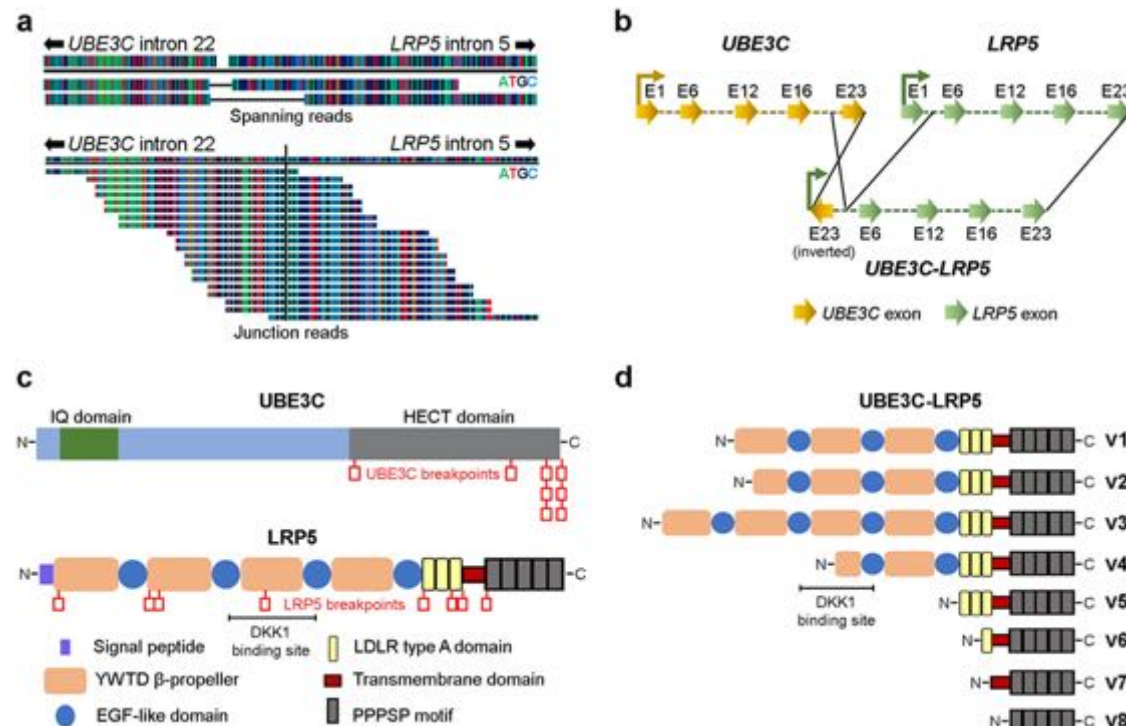
Fig. 1 | Identification of *UBE3C-LRP5* fusion variants in head and neck cancer. **a** Spanning and junction read supporting the *UBE3C-LRP5* translocation breakpoint at genomic DNA level, as detected by whole genome sequencing of the NT-8e cell line. **b** Schematic representation of *UBE3C-LRP5* fusion depicting inversion of *UBE3C* fusion partner in the fusion. Arrows represent the exons (E1–E23) along with the directionality of the gene. **c** Schematic representation of UBE3C and LRP5 protein domains and all the breakpoints identified. Red boxes indicate breakpoints identified in the NT-8e cell line, in-house HNSCC patient samples, and TCGA-HNSC data. LRP5 protein domains and the DKK1 binding site are mentioned in the schematic image. **d** Schematic representation of the predicted protein domains of the UBE3C-LRP5 (v1–v8) fusion variants identified in the NT-8e cell line, in-house HNSCC samples, and TCGA-HNSC data. The DKK1 binding site is mentioned in the schematic image.

(Fig. 1b, d). We identified two *LRP5-UBE3C* and eight *UBE3C-LRP5* fusion transcript variants. LRP5-UBE3C fusion variant proteins are predicted to harbor the extracellular Wnt binding domain of LRP5, whereas UBE3C-LRP5 fusion variant proteins are predicted to harbor the transmembrane and cytoplasmic signal transduction domains of LRP5 (Fig. 1c, d and Supplementary Fig. S6b, c).

UBE3C-LRP5 fusion stabilizes nuclear β-catenin and constitutively activates the Wnt/β-catenin pathway

To study if *LRP5-UBE3C* and *UBE3C-LRP5* fusion variants are activating, we stably overexpressed *LRP5-UBE3C* (v1) or *UBE3C-LRP5* (v1) or *UBE3C-LRP5* (v2) or *UBE3C-LRP5* (v7) fusion variants in the NIH/3T3 cell line. Overexpression of the fusion variants was confirmed by real-time PCR (Fig. 2a and Supplementary Fig. S13a). We performed a soft agar anchorage-independent growth assay with NIH/3T3 clones overexpressing fusion variants or empty vectors to check the transforming potential of the fusion transcript variants. Overexpression of *UBE3C-LRP5* (v7) was found to be the most activating, with a high number of soft agar colonies, compared to other *LRP5-UBE3C* (v1) and *UBE3C-LRP5* (v1, v2) fusion variants (Fig. 2b and Supplementary Fig. S13b). Here, we prioritized the *UBE3C-LRP5* (v7) fusion variant for functional characterization, which is referred to as the "*UBE3C-LRP5*" fusion in the manuscript. To decipher the role of the *UBE3C-LRP5* fusion in head and neck cancer, we stably overexpressed the fusion variant in the head and neck cancer cell lines, AW13516 and AW8507. Overexpression of the fusion was confirmed by real-time PCR and Western blotting (Supplementary Fig. S14a–c). As *LRP5* is a Wnt co-receptor that stabilizes β-catenin upon activation[23,24], we asked if the *UBE3C-LRP5* (v7) fusion variant constitutively activates the Wnt pathway by stabilizing nuclear β-catenin. We performed an immunofluorescence

assay to quantify the expression levels of nuclear β-catenin upon overexpression of *UBE3C-LRP5* in the AW13516 and AW8507 cell lines. The results suggest a significant increase in nuclear β-catenin expression upon overexpression of the fusion in both the head and neck cancer cell lines (Fig. 2c, d). To confirm these findings, we fractionated AW13516 and AW8507 cells, stably overexpressing *UBE3C-LRP5* fusion or vector control, and separated the nuclear and cytoplasmic fractions. Western blotting results suggested a significantly high accumulation of β-catenin in the nuclear fraction of cells upon overexpression of *UBE3C-LRP5* fusion compared to vector control cells (Fig. 2e, f). These results suggest the constitutive activation of the Wnt/β-catenin pathway. To confirm whether the pathway was activated, we screened for the expression of Wnt signaling pathway target genes (*MYC*, and *CCND1*), and co-activators (*CTNNB1*, *LEF1*, and *TCF4*). Real-time PCR-based validation for expression of these genes in AW13516- and AW8507-*UBE3C-LRP5* fusion overexpression clones showed significantly high expression of *MYC*, *CCND1*, *LEF1*, and *TCF4* upon overexpression of the fusion transcript (Supplementary Fig. S15a, b). These results indicate that *UBE3C-LRP5* fusion stabilizes nuclear β-catenin to constitutively activate the Wnt/β-catenin pathway and transform cells in vitro.

UBE3C-LRP5 fusion has transforming potential in vivo and promotes metastasis in vitro

To confirm the in vitro findings and study the role of *UBE3C-LRP5* fusion in tumorigenesis in vivo, we used a xenograft mouse model and injected NIH/3T3 clones overexpressing *UBE3C-LRP5*, along with vector control cells, subcutaneously in six mice per group. Caliper measurements at regular intervals showed that NIH/3T3 cells overexpressing the empty vector did not form tumors (0/6), whereas NIH/3T3 cells overexpressing *UBE3C-*
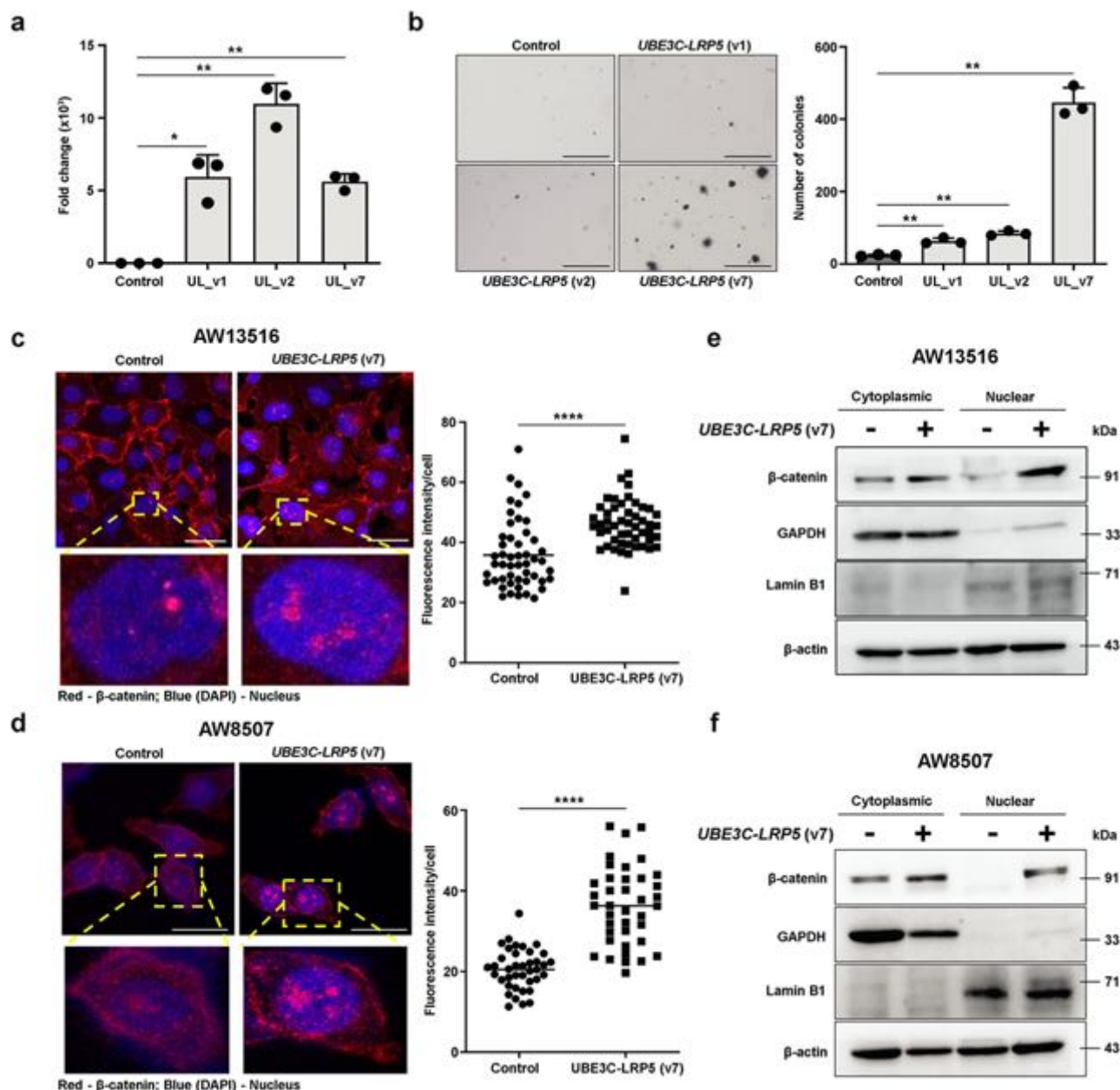
Fig. 2 | *UBE3C-LRP5* fusion stabilizes nuclear β-catenin to activate the Wnt pathway. a qRT-PCR of *UBE3C-LRP5* fusion transcript in NIH/3T3 cells stably overexpressing empty vector or *UBE3C-LRP5* (UL) fusion variants (UL_v1 or UL_v2 or UL_v7). *Gapdh* was used for the normalization of gene expression. **b** Soft agar anchorage-independent growth assay of NIH/3T3 cells stably overexpressing the empty vector or fusion transcript variants. The bar plot indicates the number of colonies in fusion overexpression clones and vector control cells. Scale bar = 400 μM. **c**, **d** Schematic representation of immunofluorescence assay performed to detect expression of nuclear β-catenin in AW13516 (**c**) and AW8507 (**d**) clones stably overexpressing empty vector or *UBE3C-LRP5* (v7) fusion. The yellow color dotted box on the images represent the magnified area of the image shown below. The nucleus is stained with DAPI (blue color) and β-catenin is stained with Alexa Fluor 633 (red color). The scatter plot representation of immunofluorescence assay data on the right indicates the fluorescence intensity/cell (*n* = 50 cells/group). Scale bar = 4 μM (**c**) and 30 μM (**d**). **e**, **f** Immunoblot of β-catenin, GAPDH, Lamin B1, and β-actin in the cytoplasmic and nuclear fractions of AW13516- (**e**) and AW8507- (**f**) clones stably expressing empty vector or *UBE3C-LRP5* (v7) fusion. The blots are from the same experiment and were processed in parallel. Data were shown as means ± SD. *p* values are from the Student's unpaired *t*-test and denoted as ns (not significant); **p < 0.05; ***p < 0.01; *****p < 0.0001. The data shown are representative of *n* = 3 independent experiments.

LRP5 fusion formed tumors in 6/6 mice (Fig. 3a), confirming the transforming potential of fusion transcripts in vitro, and in vivo. The Wnt/β-catenin pathway has been reported to regulate proliferation, migration, and invasion in head and neck cancer[25–28]. We investigated whether the *UBE3C-LRP5* fusion-activated Wnt pathway promoted these phenotypes in head and neck cancer cell lines. A clonogenic assay was performed to assess the ability of single cells to form colonies and the long-term survival of cells overexpressing fusion and vector control cells. Clonogenic assay of

AW13516- and AW8507- clones overexpressing *UBE3C-LRP5* fusion, but not the full-length *LRP5*, suggested a significant increase in the number and size of the colonies upon overexpression of the fusion compared to the vector control in both cell lines (Fig. 3b and Supplementary Fig. S16a–e). Assays were performed to investigate the role of the *UBE3C-LRP5* fusion-activated Wnt pathway in metastasis, invasion, and migration. In vitro, migration assay results suggested a significant increase in the migratory potential of AW13516, AW8507, and NIH/3T3 cells upon overexpression
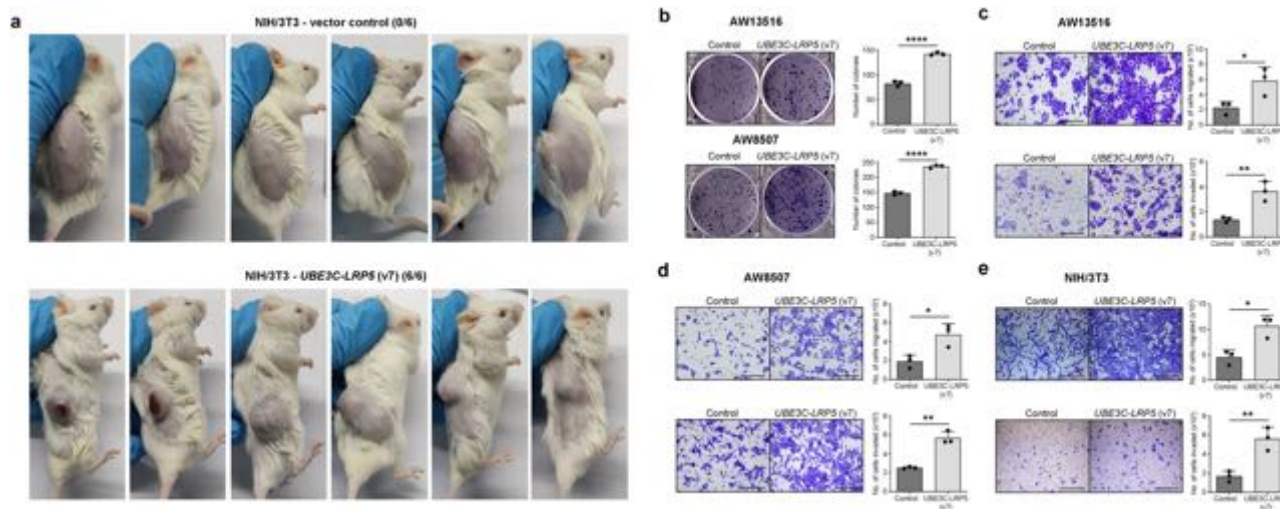
Fig. 3 | *UBE3C-LRP5* (v7) fusion has transforming potential in vivo and promotes metastasis in vitro. a In vivo tumorigenicity assay performed using NOD-SCID mice subcutaneously injected with NIH/3T3 cells stably overexpressing the empty vector (*n* = 6) or *UBE3C-LRP5* (v7) fusion variant (*n* = 6). The number of mice with the tumors is mentioned on the top of the mice images. **b** Clonogenic cell survival assay of AW13516 (top panel) and AW8507 (bottom panel) cells stably expressing empty vector or *UBE3C-LRP5*. The bar plots on the right indicate the number of colonies formed in each group. **c–e** Cell migration (top panels) and invasion assay (bottom panels) of AW13516- (**c**), AW8507- (**d**), and NIH/3T3- (**e**) cells stably expressing empty vector or *UBE3C-LRP5* (v7) fusion. The bar plots depict the number of cells migrated or invaded in vector control and *UBE3C-LRP5* (v7) fusion-expressing clones. Data were shown as means ± SD. *p* values are from the Student's unpaired *t*-test and denoted as *p < 0.05; **p < 0.01; ****p < 0.0001. The data shown are representative of *n* = 3 independent experiments. Scale bar = 400 µM.

of *UBE3C-LRP5* fusion as compared to the vector control cells (Fig. 3c–e). Furthermore, the invasion assay also suggested a significant increase in the invasive potential of AW13516, AW8507, and NIH/3T3 cells upon overexpression of the fusion (Fig. 3c–e), suggesting that *UBE3C-LRP5* fusion overexpression induces cellular proliferation, migration, and invasion. In contrast, siRNA-mediated knockdown of *UBE3C-LRP5* (v7) fusion, but not the full-length *LRP5*, in AW8507-*UBE3C-LRP5* (v7) fusion overexpression clones suppresses the clonogenic, migratory, and invasive potential of the clones (Fig. 4a, c–e and Supplementary Fig. S17). Strikingly, transient knockdown of *UBE3C-LRP5* (v1 and v2) fusion variants in the NT-8e cell line, which endogenously expresses these fusion variants, significantly reduces the clonogenic, migratory, and invasive potential of the cells (Fig. 4b, f–h). Consistently, the knockdown of *LRP5* did not affect these phenotypes in the NT-8e cell line. Taken together, these results suggest that overexpression of *UBE3C-LRP5* fusion, but not *LRP5*, is sufficient to induce tumorigenesis in vitro and in vivo and promote migration and invasion of head and neck cancer cells in vitro.

Pyrvinium pamoate inhibits *UBE3C-LRP5* activated Wnt pathway and suppresses tumor growth
To identify therapeutic drugs that target the constitutively activated Wnt/β-catenin pathway, we screened the literature and found that an FDA-approved anthelminthic drug, pyrvinium pamoate, has been reported to target β-catenin and inactivate Wnt signaling in various cancers[29–31]. To determine whether pyrvinium pamoate targets and degrades β-catenin in head and neck cancer, we treated the AW13516 and AW8507 cell lines with increasing doses of pyrvinium pamoate (0.5, 1, 2, and 3 µM) and screened for β-catenin protein expression by Western blotting. Western blotting results suggested a dose-dependent degradation of β-catenin in head and neck cancer cell lines (Supplementary Fig. S18). Furthermore, to study whether the cells overexpressing *UBE3C-LRP5* fusion are sensitive to pyrvinium pamoate, we performed an MTT assay with AW13516, AW8507, and NIH/3T3 clones overexpressing the fusion and compared them to vector control cells. MTT assay results suggested a significant increase in the sensitivity of cell lines overexpressing *UBE3C-LRP5* fusion to pyrvinium pamoate (Fig. 5a–c). We asked if NT-8e cells, which endogenously express the *UBE3C-LRP5* (v1 and v2) fusion variants, display sensitivity to pyrvinium pamoate and performed MTT

assay with the HNSCC cell lines (AW13516, AW8507, and NT-8e). Interestingly, NT-8e cells showed higher sensitivity to pyrvinium pamoate compared to other HNSCC cells without the fusion (Fig. 5d). To check the dependency of fusion-expressing cells on the Wnt/β-catenin pathway, we performed siRNA-mediated knockdown of *CTNNB1* and *LEF1*. Strikingly, we find that knockdown of *CTNNB1* or *LEF1* suppresses proliferation, and clonogenic abilities of AW8507-*UBE3C-LRP5* (v7) overexpression clones and NT-8e cells (Fig. 5e–j). Moreover, the cells display decreased sensitivity to pyrvinium pamoate upon knockdown of *CTNNB1* or *LEF1* (Fig. 5k, l), confirming the dependency of fusion-expressing cells on the Wnt/β-catenin pathway. To study the effect of pyrvinium pamoate on soft agar anchorage-independent growth, we performed an assay with NIH/3T3 cells stably overexpressing the *UBE3C-LRP5* fusion and treated them with pyrvinium pamoate (0.5 µM). Soft agar anchorage-independent assay results suggested a significant decrease in the number and size of colonies after drug treatment (Fig. 6a). To confirm the in vitro findings and study the effect of pyrvinium pamoate on tumorigenesis in vivo, we used a xenograft mouse model and subcutaneously injected 12 mice with NIH/3T3 clones overexpressing *UBE3C-LRP5*. Mice were randomly divided into two groups (*n* = 6 mice/group) for pyrvinium pamoate or vehicle treatment. Caliper measurements were taken at regular intervals to monitor the tumor and pyrvinium pamoate drug treatment (10 mg/kg dose every 48 h) was started when the tumors in mice reached 100 mm³ in size[32] in 24 days. In vivo results suggest a significant decrease in the tumor volume upon pyrvinium pamoate treatment (Fig. 6b, c and Supplementary Fig. S19). Remarkably, we noticed a distinct pattern where the tumor volume experiences a significant and abrupt escalation once it reaches the size range of 100–120 mm³ in the vehicle control group. Specifically, we observed a remarkable 5–6-fold increase in tumor volume between day 24 and day 27. To generate a visual representation of excised tumors from both the vehicle control and treatment groups, we conducted terminal sacrifice of the mice on day 33 post-injection. Additionally, we sought to assess whether pyrvinium pamoate treatment has a positive impact on the overall survival of the mice. For this purpose, we introduced NIH/3T3 clones overexpressing *UBE3C-LRP5* into a fresh set of 12 mice, which were then randomly divided into two groups, with each group comprising six mice. These groups were subjected to either
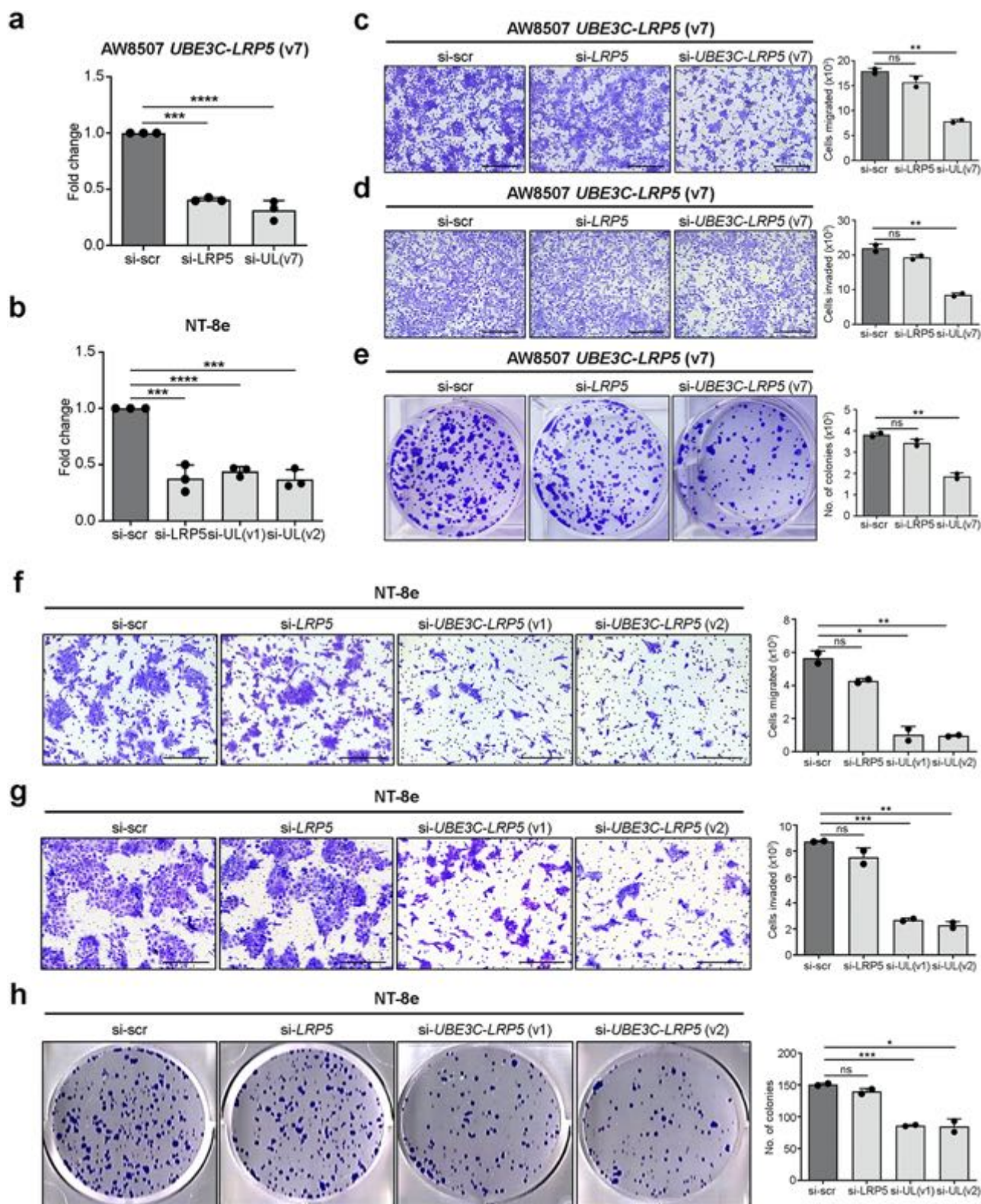
Fig. 4 | Knockdown of *UBE3C-LRP5* fusion suppresses clonogenic, migratory, invasive potential of head and neck cancer cells. a Real-time PCR of *LRP5*, and *UBE3C-LRP5* (v7) fusion variant in AW8507-*UBE3C-LRP5* (v7) clones expressing scrambled siRNA or siRNAs targeting *LRP5*, or *UBE3C-LRP5* (v7). **b** Real-time PCR of *LRP5*, and *UBE3C-LRP5* (v1 and v2) fusion variants in NT-8e cells expressing scrambled siRNA or siRNAs targeting *LRP5*, *UBE3C-LRP5* (v1), or *UBE3C-LRP5* (v2). **c, d, f, g** Boyden chamber cell migration (**c, f**) and invasion assay (**d, g**) of AW8507-*UBE3C-LRP5* (v7) (**c, d**) and NT-8e cells (**f, g**) expressing scrambled siRNA or siRNA targeting LRP5 or the *UBE3C-LRP5* fusion variants. The bar plots depict the number of cells migrated or invaded in scrambled siRNA control or siRNAs targeting *LRP5*, or UBE3C-LRP5 fusion variants. **e, h** Clonogenic cell survival assay of AW8507-*UBE3C-LRP5* (v7) (**e**) and NT-8e cells (**h**) expressing scrambled siRNA or siRNA targeting the *UBE3C-LRP5* fusion variants or *LRP5*. The bar plots on the right indicate the number of colonies formed in each group. Data were shown as means ± SD. *p* values are from the Student's unpaired *t*-test and are denoted as *ns* (not significant); *$p < 0.05$; **$p < 0.01$; ***$p < 0.001$; ****$p < 0.0001$. Scale bar = 400 μM.
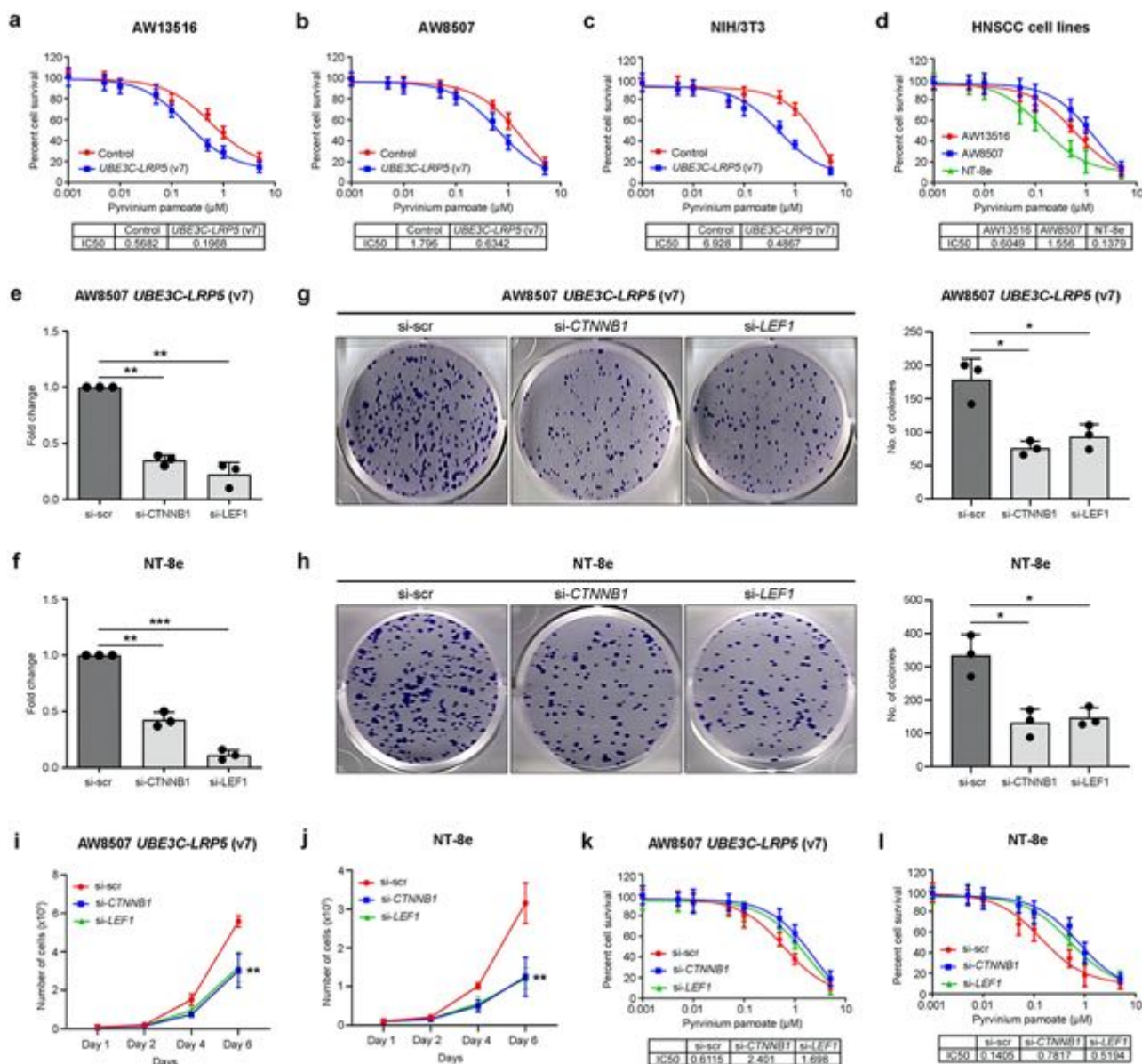
Fig. 5 | Pyrvinium pamoate treatment or knockdown of *CTNNB1* or *LEF1* inhibits *UBE3C-LRP5* activated Wnt pathway and suppresses proliferation and clonogenic ability of HNSCC cells. a–d MTT assay for assessing the response of AW13516- (**a**), AW8507- (**b**), and NIH/3T3- (**c**) clones stably expressing empty vector or *UBE3C-LRP5* and HNSCC cell lines (AW13516, AW8507, and NT-8e) (**d**) to pyrvinium pamoate. The percentage of cells surviving the treatment (y-axis) and drug concentration (x-axis) are plotted. The table at the bottom shows IC50 values (μM). **e, f** Real-time PCR of *CTNNB1*, and *LEF1* in AW8507-*UBE3C-LRP5* (v7) clones (**e**) and NT-8e (**f**) cells expressing siRNAs targeting *CTNNB1* or *LEF1* compared to the cells expressing scrambled siRNA. **g, h** Clonogenic cell survival assay of AW8507-*UBE3C-LRP5* (v7) clones (**g**), and NT-8e cells (**h**) expressing scrambled siRNA or siRNAs targeting the *CTNNB1* or *LEF1*. The bar plots on the right indicate the number of colonies formed in each group. **i, j** Cell proliferation assay of AW8507-*UBE3C-LRP5* (v7) clones (**i**) and NT-8e (**j**) expressing scrambled siRNA or siRNAs targeting the *CTNNB1* or *LEF1*. Scatter plots indicate the number of live cells on the mentioned day. **k, l** MTT assay for assessing the response of AW8507-*UBE3C-LRP5* (v7) clones (**k**), and NT-8e cells (**l**) expressing scrambled siRNA or siRNAs targeting the *CTNNB1*, or *LEF1* to pyrvinium pamoate. Data were shown as means ± SD. *p* values are from the Student's unpaired *t*-test and denoted as *$p < 0.05$; **$p < 0.01$; ***$p < 0.001$.

pyrvinium pamoate or vehicle treatment. The survival study depicts Kaplan–Meier (KM) curves at various time points following cell injection (Fig. 6d). The presence of two distinct steps in the KM curve for the vehicle control group signifies that, in the first step, $n = 4$ mice were terminally sacrificed, while $n = 2$ mice remained in the second step. These terminations were carried out in accordance with the humane endpoint criteria outlined by the Institutional Animal Ethics Committee (IAEC) at ACTREC, which considered both animal health and tumor volume. The survival analysis results suggest that pyrvinium pamoate targets β-catenin and inhibits tumor growth, thereby increasing the survival of mice injected with NIH/3T3 clones overexpressing *UBE3C-LRP5* fusion

(Fig. 6d). We investigated whether the presence of fusion transcripts affects the survival of patients with head and neck cancer. Follow-up data were available for 138 in-house HNSCC patients, and the median survival duration for the cohort was 3.3 years (ranges from 1 month to 8.5 years, as the patient samples were collected retrospectively, the follow-up period was not reached the 5-year mark in all patients). During this period, 59 recurrences, 15 distant metastases, and nine fatal events occurred. We performed Kaplan–Meier survival analysis using in-house head and neck cancer data ($n = 138$) and TCGA-HNSC data ($n = 502$). Survival analysis results showed a trend of poor survival in patients positive for fusion in the in-house data ($p = 0.078$) and TCGA-HNSC
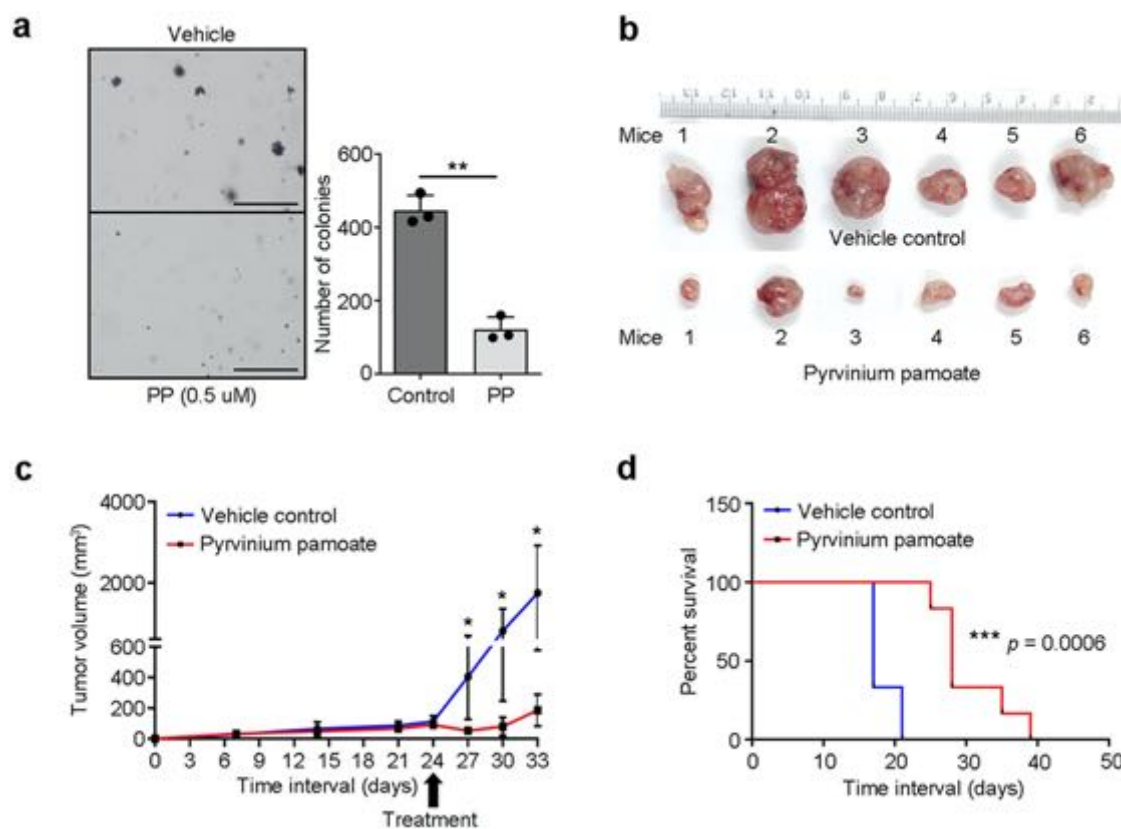
Fig. 6 | Pyrvinium pamoate treatment suppresses tumor growth and increases survival of mice injected with *UBE3C-LRP5* (v7) fusion-expressing cells. a Soft agar anchorage-independent growth assay of NIH/3T3-*UBE3C-LRP5* (v7) clones treated with vehicle or 0.5 μM pyrvinium pamoate (PP). The bar plot indicates the number of colonies in the vehicle and pyrvinium pamoate treatment arm. Data were shown as means ± SD. **b** Excised tumors from mice injected with NIH/3T3-*UBE3C-LRP5* clones, treated with vehicle or pyrvinium pamoate. **c** The graph depicts the tumor volume (y-axis) and number of days (x-axis) after injection of NIH/3T3-*UBE3C-LRP5* clones in the mice. Arrow represents the day of the start of drug treatment. Tumor volumes are shown as mean ± SEM ($n = 6$/group). **d** Kaplan–Meier survival curves for overall survival (OS) of mice treated with vehicle control (blue line) or pyrvinium pamoate (red line). The log-rank test was used to determine the statistical differences in median survival. The *p* values are from the Student's unpaired *t*-test and denoted as *$*p < 0.05$; $**p < 0.01$. Scale bar = 400 μM.

data ($p = 0.43$); however, this was not significant due to the small number of patients positive for the fusion (Supplementary Fig. S20a, b).

Discussion

The literature suggests that truncated mutant of *LRP5* with loss of the DKK1 inhibitory domain is activating in hyperparathyroid[33] and breast cancer[34]. Moreover, *LRP5* and *LRP6* mutants with loss of the extracellular domain have been reported to constitutively activate the Wnt/β-catenin pathway in a Frizzled receptor- and ligand-independent manner[35,36]. Consistent with these reports, ectopic expression of the *UBE3C-LRP5* (v7) splice variant was the most activating, with a higher number of soft agar colonies, compared to other *LRP5-UBE3C* (v1) and *UBE3C-LRP5* (v1, v2) fusion variants, possibly because of the absence of the DKK1 inhibitory domain of LRP5 in the UBE3C-LRP5 (v7) fusion. Immunofluorescence and western blot analysis of nuclear and cytoplasmic cell fractionation revealed a significantly high accumulation of β-catenin in the nuclear fraction of cells upon over-expression of *UBE3C-LRP5* fusion, indicating constitutive activation of the Wnt/β-catenin pathway with upregulated target genes, *MYC*, *CCND1*[37–39], *LEF1*, and *TCF4*[40–44] as reported in the literature for multiple cancers. We found that overexpression of *UBE3C-LRP5* fusion significantly increased the clonogenic, migratory, and invasive potential of head and neck cancer cells by activating the Wnt/β-catenin pathway, whereas transient knock-down of the fusion, but not full-length *LRP5*, suppresses these phenotypes. These results are consistent with the literature, which suggests that over-expression or knockdown of full-length *LRP* does not influence the Wnt pathway activation or transforming ability of cells in breast[34] and hyper-parathyroid cancer[33]. To validate whether the fusion transcript is

transforming in vivo, we used xenograft mouse models and subcutaneously injected fusion-expressing NIH/3T3 cells. The *UBE3C-LRP5* fusion tran-script transformed NIH/3T3 cells in vivo, forming subcutaneous tumors in 100% of mice injected with cells stably expressing the fusion transcript compared to 0% in mice injected with cells expressing the empty vector. Thus, our findings indicate that *UBE3C-LRP5* fusion activates in vitro and in vivo, promoting proliferation, migration, and invasion of head and neck cancer cells.

Although no drugs have been approved for targeting *LRP5*, we eval-uated a known FDA-approved anthelminthic drug, pyrvinium pamoate, which degrades β-catenin to inactivate the Wnt pathway[29–31,45]. Head and neck cancer cells expressing *UBE3C-LRP5* fusion transcripts were sensitive to pyrvinium pamoate, which degrades β-catenin in a dose-dependent manner. Moreover, endogenously fusion-expressing NT-8e cells showed higher sensitivity to pyrvinium pamoate compared to other HNSCC cells without the fusion. Interestingly, the knockdown of *CTNNB1*, or *LEF1*, in fusion-expressing cells reduced the sensitivity of the cells to pyrvinium pamoate, confirming their dependency on the Wnt/β-catenin pathway. Furthermore, soft agar anchorage-independent assay suggested inhibition of the transforming ability of cells upon treatment with the inhibitor, as reported for cells with activated Wnt/β-catenin pathway[46–48]. Consistent with the in vitro findings, in vivo xenograft assay results suggest a significant reduction in the tumor volume of mice bearing tumors of NIH/3T3 cells overexpressing the fusion upon treatment with pyrvinium pamoate as reported in various cancers with activated Wnt/β-catenin pathway, including glioblastoma and breast cancer[30,45,49,50]. Similarly, when treated with pyrvinium pamoate, mice bearing tumors of fusion overexpression

clones showed significantly better overall survival than those treated with vehicle control[30]. Importantly, in-house HNSCC data showed a trend towards poor survival of fusion-positive patients, wherein statistical significance could not be attained due to inadequate sample size, similar to the *NTRK* fusions[51].

In summary, our study presents the functional and clinical significance of a fusion transcript between the E3 ubiquitin ligase, *UBE3C*, and the Wnt signaling co-receptor, *LRP5*, found in a subset of patients with head and neck cancer. The *UBE3C-LRP5* fusion transcript transforms in vitro and in vivo, promoting proliferation, migration, and invasion of head and neck cancer cells through constitutive activation of the Wnt/β-catenin pathway. The UBE3C-LRP5 fusion protein and the Wnt pathway can be targeted by the FDA-approved anthelminthic drug pyrvinium pamoate, which degrades β-catenin to inactivate the pathway, leading to a reduction in the anchorage-independent growth of cells and tumor volume in mice bearing tumors of fusion overexpression clones. Importantly, mice treated with pyrvinium pamoate also showed significantly better overall survival than those treated with vehicle control. Further studies are needed to validate the clinical significance of this fusion in larger patient cohorts and to assess the efficacy and safety of pyrvinium pamoate in patients with head and neck cancer. Overall, this study underscores the importance of continued research on the molecular drivers of cancer and the development of targeted therapies that can improve patient outcomes. Specifically, investigating whether the *UBE3C-LRP5* (v7) fusion variant mimics truncated *LRP5* could yield further valuable insights[33,34].

The limitations of this study include the low activity of pyrvinium pamoate on head and neck cancer cell lines, its retrospective design, and the lack of samples positive for the fusion transcripts, which led to inconclusive results in the survival analysis. Designing a prospective study with a large cohort of patients is warranted to provide detailed information on fusion gene prevalence, correlation with clinicopathological features and patient survival, and establish *UBE3C-LRP5* fusion as a therapeutic target in head and neck cancer.

Methods
Patient sample details
A total of 151 fresh-frozen head and neck tumor samples were used to identify and validate the fusion transcripts. The patient details are provided in Table 1. The patient details include age, gender, anatomic site, TNM tumor stage (as per the 8th edition of AJCC (American Joint Committee on Cancer)/ UICC (Union for International Cancer Control) TNM classification system), nodal status, smoking (representing the patients with habits of smoking tobacco such as cigarettes, cigars, or pipes), chewing, alcohol, tobacco (representing the patients with the habit of smoke-less tobacco chewing), recurrence, metastasis, and status at the last follow-up.

Ethical approval
The study was conducted according to the guidelines of the Declaration of Helsinki and approved by the Institutional Review Board (IRB) and Ethics Committee (EC) of the Tata Memorial Centre-ACTREC. All patient samples were collected from the tumor tissue repository (TTR) of Tata Memorial Hospital (TMH) and the biorepository of Advanced Centre for Treatment, Research, and Education in Cancer (ACTREC), Mumbai, which routinely collects and maintains fresh-frozen tumor and normal tissue samples of cancer patients for research use. As the samples were collected retrospectively, the IRB and EC waived the need for informed consent. This is a routine procedure followed at the TMH and ACTREC.

Cell culture
AW13516[52], AW8507[52], NT-8e[53], and OT9[53,54] head and neck cancer (HNSCC) cell lines[55,56] were obtained from Tata Memorial Hospital (Mumbai), while the NIH/3T3 (CRL-1658) cell line was procured from the American Type Culture Collection (ATCC). The cell lines were authenticated by DNA short tandem repeat (STR) profiling using the Promega Geneprint 10 system in conjugation with the GeneMarker HID software

tool. HNSCC cell lines were cultured in Dulbecco's Modified Eagle Medium (DMEM) (cat. no. 12800 – 017; Gibco), supplemented with 10% fetal bovine serum (FBS) (cat. no. 10270106; Gibco) and 1.25 μl/ml gentamycin (Abbott). NIH/3T3 cells were cultured in DMEM supplemented with 10% bovine calf serum (BCS) (cat. no. SH30073.03; Cytiva HyClone) and 1.25 μl/ml gentamycin. Cells were tested for mycoplasma and found to be negative, but as a standard lab protocol, we treated the cells using EZKill Mycoplasma Removal Reagent (cat. no. CCK006 – 1; HiMedia) every 6 months.

DNA/RNA extraction, RT-PCR, and real-time PCR
RNA was extracted from the tissue samples using the AllPrep DNA/RNA/miRNA Universal Kit (cat. no. 80224; QIAGEN). Approximately 20–30 mg of tissue sections were cut into small pieces, subjected to bead-based homogenization in 600 μL lysis buffer using a FastPrep homogenizer (MP Biomedicals, USA), and further processed for total RNA extraction according to the manufacturer's protocol. Total RNA was extracted from the cell lines using the TRIzol reagent (cat. no. T9424; Sigma-Aldrich).

Table 1 | Clinical characteristics of 151 patients in the study

Clinicopathological features	Variable	Frequency (*n* = 151), *n* (%)
Age	Median (range)	44 (23–76)
	<40	49 (32%)
	40–60	64 (42%)
	>60	25 (17%)
	NA	13 (9%)
Gender	Male	111 (74%)
	Female	27 (18%)
	NA	13 (9%)
Anatomic site	Tongue	150 (99%)
	Buccal mucosa	1 (1%)
TNM Tumor stage	pT1-T2	114 (75%)
	pT3-T4	37 (25%)
Nodal Status	Node positive	85 (56%)
	Node negative	66 (44%)
Smoking	Smoker	40 (26%)
	Non-smoker	98 (65%)
	NA	13 (9%)
Chewing	Chewer	100 (66%)
	Non-chewer	38 (25%)
	NA	13 (9%)
Alcohol	Yes	32 (21%)
	No	106 (70%)
	NA	13 (9%)
Tobacco	Yes	102 (68%)
	No	36 (24%)
	NA	13 (9%)
Recurrence	Yes	59 (39%)
	No	79 (52%)
	NA	13 (9%)
Metastasis	Yes	15 (10%)
	No	123 (81%)
	NA	13 (9%)
Status at last follow-up	Alive	129 (85%)
	Died	9 (6%)
	NA	13 (9%)

NA information not available

According to the manufacturer's instructions, genomic DNA from the cell lines was extracted using the QIAamp DNA Blood Mini Kit (cat. no. 51106; QIAGEN). The RNA/DNA concentration was measured using a Nano-Drop 2000c spectrophotometer (Thermo Fisher Scientific). About 2 µg total RNA from tumor and normal tissues was used for cDNA synthesis using the PrimeScript TM first strand cDNA synthesis kit (cat. no. RR370A; TaKaRa) according to the manufacturer's protocol. About 10 ng of cDNA was used for PCR amplification using a KAPA Taq PCR kit (cat. no. KK1024; KAPA Biosystems) in a 10 µl reaction containing fusion-specific forward and reverse primers or GAPDH primers (2 pmol), followed by gel-purification, and Sanger sequencing. The details of all primers used for the fusion transcript validation are provided in Supplementary Table S1. Quantitative real-time PCR was performed using the KAPA SYBR real-time PCR master mix (cat. no. KK4601; KAPA Biosystems) on a QuantStudio 12 K Flex Real-Time PCR System (cat. no. 4470935; Applied Biosystems). For quantitative real-time PCR of each sample, 6 µL reactions in triplicate were incubated in a 384-well plate at 95 °C for 5 min, followed by 40 cycles of 95 °C for 15 s, 64 °C for 15 s, and 72 °C for 15 s. Primer sequences used for real-time PCR validation of genes are provided in Supplementary Table S2. All real-time PCR experiments were performed in triplicate.

Transcriptome sequencing and fusion analysis
Transcriptome sequencing of 15 head and neck cancer patient samples and four cell lines was performed to identify the fusion transcripts. Transcriptome sequencing libraries were constructed using the TruSeq RNA library protocol. Briefly, mRNA was purified from 4 µg of intact total RNA using oligodT beads, and library preparation was performed according to the manufacturer's protocol (TruSeq RNA Sample Preparation Kit, Illumina). Chimerascan[57] was used to identify transcript fusion following the default parameters in the tumor, normal, and cell lines. For fusion mapping, paired-end raw read sequences were mapped to human reference genome sequences (hg19). Using scripts developed in-house in Python, we filtered fusion pairs without spanning read support, transcript allele fraction (TAF) <0.01, for both the partner, pseudogenes, and homologous sequences spanning reads, as described previously[58]. Tumor-specific fusions were further processed for annotation using Oncofuse[59], and the frame of fusion was determined. The upstream and downstream sequences supporting fusion were retrieved, and primers were designed using Primer-BLAST[60].

TCGA-HNSC data fusion analysis
The RNA-seq tier 1 data (aligned BAM files) of the TCGA-HNSC project (n = 502) were downloaded from the National Cancer Institute Cancer Genome Commons Portal (http://portal.gdc.cancer.gov). The BAM files were converted to raw fastq files using the SamToFastq utility of the Picard toolkit (https://broadinstitute.github.io/picard/) as described previously[61]. Primary alignment of the transcriptome data was performed against GRCh38 (GRCh.p12 GENCODE v30) using the two-pass mode of the STAR aligner (v2.7.6a)[62]. Discordant and split reads mapping to *LRP5*/ *UBE3C* genomic coordinates were extracted and annotated using in-house custom scripts. The reads supporting the breakpoints were manually superimposed to derive contigs.

Whole genome sequencing and SvABA analysis
The whole genome sequencing (WGS) library was prepared using the Illumina-compatible NEXTflex Rapid DNA Sequencing Bundle (5144 – 02, NEXTflex, BIOO Scientific, Inc. USA). Briefly, 300 ng of Qubit-quantified DNA was sheared in a Covaris microTUBE AFA (520045, Life Technologies) using a Covaris S220 sonicator (4465653, Life Technologies, Covaris, Inc. USA) to generate fragments with a size range of 300–400 bp. Fragment size distribution was verified using an Agilent 2100 Bioanalyzer and purified using HighPrep magnetic beads (AC-60050, MagBio Genomics, Inc., USA). Purified fragments were end-repaired, adenylated, and ligated to Illumina multiplex barcode adapters according to the NEXTflex Rapid DNA sequencing bundle kit protocol. The adapter-ligated DNA was purified using HighPrep beads. The resultant fragments were amplified for five

cycles of PCR using Illumina-compatible primers provided in the NEXTflex Rapid DNA sequencing Bundle. The final PCR product (sequencing library) was purified using HighPrep beads, followed by quality control of the library. The sequencing library was quantified using a Qubit fluorometer (Thermo Fisher Scientific, MA, USA), and the fragment size distribution was analyzed using an Agilent 2100 Bioanalyzer (5067 – 4626, Agilent High Sensitivity DNA Bioanalyzer Kit). Whole genome sequencing data of the NT-8e cell line were aligned to the human reference genome (GRCh38.p12 GENCODE v30) using BWA-MEM (v0.7.17)[63]. The BAM files were further analyzed using SvABA (v1.1.3)[64] to identify translocation breakpoints. The translocation breakpoints were annotated using custom scripts, using the reference GENCODE GTF (v30)[65]. The translocation breakpoints identified in the SvABA analysis were additionally confirmed using MANTA (v1.6.0)[66].

Protein extraction and western blotting
Cells were lysed using radioimmunoprecipitation assay (RIPA) lysis buffer (cat. no. R0278; Sigma-Aldrich) containing a protease inhibitor cocktail (cat. no. P8340; Sigma-Aldrich) and 0.1 M DTT. After intermittent tapping and vortexing of the samples on ice for 30 min, cell debris was pelleted by centrifugation at 14,000 rpm for 40 min, and the supernatant was collected. For Western blotting, 50 µg of protein was loaded onto an SDS-PAGE gel and transferred onto a PVDF membrane (cat. no. 10600021; Amersham Hybond, GE Healthcare). Blocking was performed using 5% BSA to avoid nonspecific antibody binding. Primary antibodies were diluted in 3% BSA and incubated overnight at 4 °C. The primary antibodies against LRP5 (cat. no. sc-390267; 1:1000; Santa Cruz Biotechnology), DYKDDDDK tag (cat. no. 8146; 1:2000; Cell Signaling Technology), β-Tubulin (cat. no. 2128; 1:2000; Cell Signaling Technology), β-catenin (cat. no. ab32572; 1:2000; Abcam), Lamin B1 (cat. no. sc-374015; 1:1000; Santa Cruz Biotechnology), GAPDH (cat. no. sc-32233; 1:2000; Santa Cruz Biotechnology), Vinculin (cat no. 4650; 1:1000; Cell Signaling Technology), and β-actin (cat. no. sc-47778; 1:2000; Santa Cruz Biotechnology) were used for Western blotting. The membranes were then washed with 1X TBST and incubated with goat anti-rabbit HRP labeled (cat. no. sc-2004; 1:2000; Santa Cruz Biotechnology) or goat anti-mouse HRP labeled (cat. no. sc-2005; 1:2000; Santa Cruz Biotechnology) antibodies for 1 h at room temperature (RT) followed by washing with TBST thrice for 15 min. The ECL Western Blotting Substrate (cat. no. T7101A; TAKARA) was used to visualize luminescence using the Chemidoc system (Bio-Rad). Nuclear and cytoplasmic fractionation was performed as described previously[67], and Western blotting was performed using 50 µg protein from each fraction. All Western blot analyses were performed in triplicate. The uncropped raw western blot images (Supplementary Fig. S21–S28) are provided in the Supplementary Information.

Cloning of *LRP5-UBE3C* and *UBE3C-LRP5* fusion cDNA
cDNA of *LRP5-UBE3C* (v1) and *UBE3C-LRP5* (v1, v2, and v7) fusion transcript variants were amplified from the NT-8e cell line using KAPA Taq DNA polymerase (cat. no. KK1024; Sigma-Aldrich) and cloned into the pTZ57R/T cloning vector (InsTAclone PCR cloning kit, cat. no. K1214R; Thermo Fisher Scientific) or pJET 1.2 blunt cloning vector (CloneJET PCR cloning kit, cat. no. K1231; Thermo Fisher Scientific), respectively, as per manufacturer's protocol. Full-length fusion cDNA sequences (Supplementary Table S3) were confirmed by Sanger sequencing. *LRP5-UBE3C* (v1), *UBE3C-LRP5* (v1, v2) fusion variants were sub-cloned into a retroviral expression vector, pBABE-puro (Addgene plasmid #1764)[68], and *UBE3C-LRP5* (v7) fusion variant was sub-cloned into a lentiviral expression vector, pLVX-AcGFP1-N1 (plasmid was obtained as a kind gift from Dr. Sagar Sengupta, NII, New Delhi), using restriction digestion-based cloning. The start and stop codons of the fusion transcript cDNAs are highlighted in green and red color, respectively, Supplementary Table S3. Primers used for cloning are listed in Supplementary Table S4.

siRNA synthesis by in vitro transcription

Sense and anti-sense DNA oligonucleotides for *UBE3C-LRP5* fusion variants (v1, v2, and v7), *LRP5, CTNNB1, LEF1*, and scrambled siRNA (Supplementary Table S5) were ordered from Sigma-Aldrich. The protocol for the synthesis of small RNA transcripts using T7 RNA polymerase is reported in the literature[69]. For each in vitro transcription (IVT) reaction, 1 nmol of each oligonucleotide (re-suspended in 1X TE buffer (10 mM Tris-HCl pH 8.0 and 1 mM EDTA)) was annealed using thermocycler to obtain double-stranded DNA (dsDNA). The thermocycler conditions used were: 95 °C for 3 min, followed by 70 cycles of 95 °C for 30 s (−1 °C/cycle). In vitro transcription (IVT) reaction was performed in 20 µL of a reaction containing 1X T7 transcription buffer (cat. no. P118B, Promega), 1X biotin RNA labeling mix (cat. no. 11685597910, Sigma-Aldrich), 1 U RiboLock RNase Inhibitor (cat. no. EO0381, Fermentas), 10 U T7 RNA polymerase (cat. no. P2075, Promega), and 1 nmol of dsDNA, as a template. The reaction was incubated at 37 °C for 2 h. Sense and anti-sense small interfering RNA (siRNA) synthesized in separate reactions were annealed by mixing the transcription reactions at 95 °C for 1 min, followed by 70 cycles of 95 °C for 30 s (−1 °C/cycle) to obtain double-stranded siRNAs.

Overexpression and knockdown studies

For stable overexpression of *LRP5-UBE3C* (v1) fusion, the pBABE-puro-*LRP5-UBE3C* construct was used. For stable overexpression of *UBE3C-LRP5* fusion variants (v1, v2, and v7), the constructs cloned in pBABE-puro or pLVX-AcGFP1-N1 were used. Cells with the empty vector were used as a control for overexpression. For retroviral production, 293FT cells were seeded in a six-well plate, a day before transfection, and each of the retroviral constructs, along with the packaging vector, pCL-Ampho, were transfected using Lipofectamine kit (cat. no. L3000 – 015; Invitrogen). For lentiviral production, 293FT cells were seeded in a six-well plate, a day before transfection, and the lentiviral construct, along with the packaging vectors, VSV-G and psPAX2, were transfected using a Lipofectamine kit. The viral soup was collected 48 and 72 h post-transfection, and passed through the 0.45 µM filter for removal of cells/cell debris. Target cells for transduction were seeded 1 day before transduction in a six-well plate and allowed to grow to reach 50–60% confluency. One milliliter of the virus soup (1:1 dilution) and 8 µg/ mL of polybrene (cat. no. H9268, Sigma-Aldrich) was added to cells and incubated for 6 h. Positive clones were selected using 0.5 µg/ml of puromycin treatment (cat. no. TC198; Himedia). For transient overexpression of *LRP5*, pcDNA3.3 ss-3xFLAG-hLRP5 plasmid was used, which was a gift from Harald Junge (Addgene plasmid # 115788)[70]. Transient transfection was performed by using a Lipofectamine kit and cells were collected after 48 h for RNA isolation, protein extraction, and to perform cell-based assays. siRNA-mediated transient knockdown of *UBE3C-LRP5* (v1, v2 and v7), *LRP5, CTNNB1*, or *LEF1* was performed with siRNAs synthesized using T7 RNA polymerase. Following siRNA transfection for 48 h using Lipofectamine RNAiMAX (cat. no. 13778075, Invitrogen), cells were used for RNA isolation and in vitro cell-based assays.

Boyden chamber invasion and migration assay

Boyden chamber Matrigel invasion assays were performed using 24-well Transwell inserts (cat. no. 353097; Corning) coated with 100 µg Matrigel (cat. no. 354234; Corning) and allowed to settle for 16 h at 37 °C in 5% CO_2 incubator. Invasion assay was performed with 2×10^5 cells of AW13516-*UBE3C-LRP5* (v7) clones; 1×10^5 cells of AW8507-*UBE3C-LRP5* (v7) clones, and AW8507-*UBE3C-LRP5* (v7) clones with siRNA knockdown; 0.5×10^5 cells of NIH/3T3-*UBE3C-LRP5* (v7) clones; and 1×10^5 cells of NT-8e with siRNA knockdown suspended in 300 µL serum-free medium and seeded in the Boyden chamber and 700 µL of 10% serum-containing DMEM medium was added in the companion plate wells. For the migration assay, cells were seeded directly in a Boyden chamber without matrigel. For migration assay, 1×10^5 cells of AW13516-*UBE3C-LRP5* (v7) clones; 0.5×10^5 cells of AW8507-*UBE3C-LRP5* (v7) clones, and AW8507-*UBE3C-LRP5* (v7) clones with siRNA knockdown; 0.25×10^5 cells of NIH/3T3-*UBE3C-LRP5* (v7) clones; and 0.5×10^5 cells of NT-8e with siRNA

knockdown were used. The cells were allowed to invade/migrate for 48 h at 37 °C in a 5% CO_2 incubator. The transwell chambers were fixed and stained with 0.1% crystal violet. The membrane was mounted using DPX mountant (cat. no. 18404; Qualigens) on a slide, the invaded/migrated cells were imaged using an upright microscope at 10X magnification. Images from ten random fields were chosen, and the number of cells was counted using the ImageJ cell counter plugin tool and plotted as percent cell invasion or percent cell migration. All experiments were independently repeated thrice with two inserts per clone in each experiment (a total of six replicates per clone).

Clonogenic survival assay

Two hundred and fifty cells per well were seeded in a six-well plate (in triplicates for each clone) and incubated for 15–18 days till colonies with >50 cells per colony appeared. Colonies were fixed with 4% paraformaldehyde, stained with 0.1% crystal violet, and counted under the microscope to determine percent survival. All experiments were performed in triplicate.

Cell proliferation assay

Cell proliferation assay was performed in triplicates in 24-well plates with 10,000 cells/well for all the experiments. Cell growth was assessed on days 1, 2, 4, and 6 by passaging and counting viable cells by trypan blue staining and using a hemocytometer. All experiments were performed three times, with each experiment performed in triplicates.

Soft agar colony formation assay

Approximately 1 mL of 2X DMEM supplemented with 20% FBS containing 1 mL of 1.6% agar (to obtain 0.8% agar) was added to the six-well plate as bottom agar and solidified. Cells (1×10^4) were supplemented with 1 mL of 2X DMEM containing 0.8% agar to obtain 0.4% agar and were added to the bottom agar as the top agar. Cells were fed 250 µL of medium every 5 days and incubated for two weeks at 37 °C and 5% CO_2. Cells were stained with 0.01% crystal violet, and from each well randomly, ten field images were taken using a phase-contrast inverted microscope. Colonies were counted manually.

Immunofluorescence assay

The cells were seeded on sterile coverslips and incubated for 24 h in a CO_2 incubator. Cells were washed with 1X PBS and fixed with 4% paraformaldehyde for 15 min at room temperature (RT), washed with 1X PBS, and permeabilized with 0.5% Triton X-100 for 15 min at RT. After subsequent washing with 1X PBS, the cells were incubated for 1 h at 37 °C in 3% bovine serum albumin solution. The cells were then incubated with primary antibody: β-catenin (ab32572, 1:500; Abcam) overnight at 4 °C. After washing with 1X PBS, the coverslips were incubated with Alexa Fluor 633-conjugated goat anti-rabbit secondary antibody (cat. no. A-21070; Invitrogen) for 45 min at RT. Nuclei were counterstained with 0.5 µg/ml DAPI (cat. no. D1306; Invitrogen) for 1 min, washed thrice with 1X PBS, and mounted using VECTASHIELD antifade mounting media (cat. no. H-1000; Vector laboratories). The cells were visualized under a Zeiss LSM 510 Meta Confocal Microscope, and the staining intensities were analyzed using the ImageJ software (NIH, Bethesda, MD).

Inhibitor studies

The Wnt pathway inhibitor pyrvinium pamoate (cat. no. P0027; Sigma-Aldrich) was reconstituted in dimethyl sulfoxide (DMSO). For Western blotting (0.5, 1, 2, and 3 µM), soft agar (0.5 µM), and in vivo assays (10 mg/kg), cells were treated with the mentioned concentration of drug and collected at appropriate time points for protein isolation or colony counting.

MTT assay

Cells (2×10^3 cells per well) were seeded in a 96-well plate, incubated with pyrvinium pamoate (six replicates per concentration) for 72 h, and subsequently incubated with 0.5 mg/ml of MTT (cat. no. TC191; HiMedia) for 3 h. MTT assay data were acquired at 562 nm using a microplate reader. The

percentage of cell viability was calculated in comparison with the vehicle control. All assays were performed in triplicate.

In vivo study

All in vivo experiments were performed as approved by the Institutional Animal Ethics Committee (IAEC), TMC-ACTREC. Stable clones of NIH/3T3 overexpressing *UBE3C-LRP5* fusion or empty vector were trypsinized and suspended in 40 μL sterile 1X PBS. Cells were injected subcutaneously (three million cells/mouse) into 6–8-week-old male NOD-SCID (non-obese diabetic/severe combined immunodeficiency) mice (n = 6/group). Caliper measurements were performed every three days to monitor the tumor volumes. For both the inhibitor and survival studies, we performed two separate sets of experiments, with each set comprising a total of 12 mice. In each of these experiments, we injected three million NIH/3T3 cells over-expressing the *UBE3C-LRP5* fusion clones subcutaneously into 6–8-week-old NOD-SCID mice (n = 6/group) and were grouped to receive pyrvinium pamoate (10 mg/kg) or vehicle. Treatment was given to mice orally using oral gavage at intervals of 48 h for 9 days after the tumor volume reached 100 mm^3 (24 days after cell injection). The treatment response was monitored every three days by measuring the tumor volume using a Vernier caliper.

Survival analysis

Survival analysis was performed using the Kaplan–Meier plotter online tool[71] in the in-house and TCGA-HNSC samples. Patient clinical data were imported into the Kaplan–Meier plotter server using the custom data option. *UBE3C-LRP5* fusion status (with or without fusion) was assigned to the samples assessed in the survival analysis.

Statistics and reproducibility

Statistical analysis was performed using GraphPad Prism version 8 (GraphPad Software, La Jolla, CA, USA). Student's unpaired *t*-test was used to determine the statistical significance between different groups, and the *p* values calculated are denoted as ns (not significant); *$p < 0.05$; **$p < 0.01$; ***$p < 0.001$; ****$p < 0.0001$. The reproducibility of the experimental findings was confirmed by performing n = 3 independent replicates. The results of all the biological replicates were consistent.

Reporting summary

Further information on research design is available in the Nature Research Reporting Summary linked to this article.

Data availability

The raw sequencing data generated and analysed during the current study are available from the ArrayExpress repository (http://www.ebi.ac.uk/arrayexpress/), hosted by the European Bioinformatics Institute (EBI), under the following accession numbers: E-MTAB-3958: transcriptome sequencing data of cell lines, E-MTAB-4654: transcriptome sequencing data of tissue samples, E-MTAB-12534: whole genome sequencing data of NT-8e cell line (AD2880).

References

1. Taniue, K. & Akimitsu, N. Fusion genes and RNAs in cancer development. *Noncoding RNA* **7**, 10 (2021).
2. Latysheva, N. S. & Babu, M. M. Discovering and understanding oncogenic gene fusions through data intensive computational approaches. *Nucleic Acids Res.* **44**, 4487–4503 (2016).
3. Kheder, E. S. & Hong, D. S. Emerging targeted therapy for tumors with NTRK fusion proteins. *Clin. Cancer Res.* **24**, 5807–5814 (2018).
4. Doebele, R. C. et al. Entrectinib in patients with advanced or metastatic NTRK fusion-positive solid tumours: integrated analysis of three phase 1–2 trials. *Lancet Oncol.* **21**, 271–282 (2020).
5. Drilon, A. et al. Safety and antitumor activity of the multitargeted Pan-TRK, ROS1, and ALK inhibitor entrectinib: combined results from two phase I trials (ALKA-372-001 and STARTRK-1). *Cancer Discov.* **7**, 400–409 (2017).
6. Camidge, D. R. et al. Updated efficacy and safety data and impact of the EML4-ALK fusion variant on the efficacy of alectinib in untreated ALK-positive advanced non–small cell lung cancer in the global phase III ALEX study. *J. Thorac. Oncol.* **14**, 1233–1243 (2019).
7. Drilon, A. et al. Efficacy of selpercatinib in RET fusion–positive non–small-cell lung cancer. *N. Engl. J. Med.* **383**, 813–824 (2020).
8. Drilon, A. et al. Selpercatinib in patients with RET fusion–positive non–small-cell lung cancer: updated safety and efficacy from the registrational LIBRETTO-001 phase I/II trial. *J. Clin. Oncol.* **41**, 385–394 (2023).
9. Mullard, A. BRAF plus MEK inhibitor combo secures tumour-agnostic FDA approval. *Nat. Rev. Drug Discov.* **21**, 548 (2022).
10. Gouda, M. A. & Subbiah, V. Precision oncology for BRAF-mutant cancers with BRAF and MEK inhibitors: from melanoma to tissue-agnostic therapy. *ESMO Open* **8**, 100788 (2023).
11. Chmielecki, J. et al. Comprehensive genomic profiling of pancreatic acinar cell carcinomas identifies recurrent RAF fusions and frequent inactivation of DNA repair genes. *Cancer Discov.* **4**, 1398–1405 (2014).
12. Lemery, S. et al. Development of tissue-agnostic treatments for patients with cancer. *Ann. Rev. Cancer Biol.* **6**, 147–165 (2022).
13. Sung, H. et al. Global cancer statistics 2020: GLOBOCAN estimates of incidence and mortality worldwide for 36 cancers in 185 countries. *CA Cancer J. Clin.* **71**, 209–249 (2021).
14. Pfister, D. G. et al. Head and neck cancers, version 1.2015. *J. Natl Compr. Cancer Netw.* **13**, 847–856 (2015).
15. Beck, T. N. & Golemis, E. A. Genomic insights into head and neck cancer. *Cancers Head Neck* https://doi.org/10.1186/s41199-016-0003-z (2016).
16. Persson, M. et al. Recurrent fusion of MYB and NFIB transcription factor genes in carcinomas of the breast and head and neck. *Proc. Natl Acad. Sci. USA* **106**, 18740–18744 (2009).
17. Daly, C. et al. FGFR3-TACC3 fusion proteins act as naturally occurring drivers of tumor resistance by functionally substituting for EGFR/ERK signaling. *Oncogene* **36**, 471–481 (2016).
18. Guo, T. et al. Characterization of functionally active gene fusions in human papillomavirus related oropharyngeal squamous cell carcinoma. *Int. J. Cancer* **139**, 373–382 (2016).
19. Bossi, P. et al. Are fusion transcripts in relapsed/metastatic head and neck cancer patients predictive of response to anti-EGFR therapies? *Dis. Markers* **2017**, 1–9 (2017).
20. Cheng, Y., Wang, Y., Li, J., Chang, I. & Wang, C.-Y. A novel read-through transcript JMJD7-PLA2G4B regulates head and neck squamous cell carcinoma cell proliferation and survival. *Oncotarget* **8**, 1972–1982 (2016).
21. Tamai, K. et al. LDL-receptor-related proteins in Wnt signal transduction. *Nature* **407**, 530–535 (2000).
22. Chu, B. W. et al. The E3 ubiquitin ligase UBE3C enhances proteasome processivity by ubiquitinating partially proteolyzed substrates. *J. Biol. Chem.* **288**, 34575–34587 (2013).
23. Liu, J. et al. Wnt/β-catenin signalling: function, biological mechanisms, and therapeutic opportunities. *Signal Transduct. Target. Ther.* https://doi.org/10.1038/s41392-021-00762-6 (2022).
24. Reyes, M., Flores, T., Betancur, D., Peña-Oyarzún, D. & Torres, V. A. Wnt/β-catenin signaling in oral carcinogenesis. *Int. J. Mol. Sci.* **21**, 4682 (2020).
25. Sato, K., Okazaki, Y., Tonogi, M., Tanaka, Y. & Yamane, G.-Y. Expression of β-catenin in rat oral epithelial dysplasia induced by 4-nitroquinoline 1-oxide. *Oral Oncol.* **38**, 772–778 (2002).
26. Suzuki, H. et al. Clinical significance of altered expression of β-catenin and E-cadherin in oral dysplasia and cancer: potential link with ALCAM expression. *PLoS ONE* **8**, e67361 (2013).

27. Reyes, M., Peña-Oyarzun, D., Maturana, A. & Torres, V. A. Nuclear localization of β-catenin and expression of target genes are associated with increased Wnt secretion in oral dysplasia. *Oral Oncol.* **94**, 58–67 (2019).

28. Ishida, K. et al. Nuclear localization of beta-catenin involved in precancerous change in oral leukoplakia. *Mol. Cancer* https://doi.org/10.1186/1476-4598-6-62 (2007).

29. Hu, Z. et al. KIF3A inhibits nasopharyngeal carcinoma proliferation, migration and invasion by interacting with beta-catenin to suppress its nuclear accumulation. *Am. J. Cancer Res.* **12**, 5226–5240 (2022).

30. Li, H. et al. Pyrvinium pamoate regulates MGMT expression through suppressing the Wnt/β-catenin signaling pathway to enhance the glioblastoma sensitivity to temozolomide. *Cell Death Discov.* https://doi.org/10.1038/s41420-021-00654-2 (2021).

31. Thorne, C. A. et al. Small-molecule inhibition of Wnt signaling through activation of casein kinase 1α. *Nat. Chem. Biol.* **6**, 829–836 (2010).

32. Li, B. et al. Pyrvinium attenuates hedgehog signaling downstream of smoothened. *Cancer Res.* **74**, 4811–4821 (2014).

33. Bjorklund, P., Akerstrom, G. & Westin, G. An LRP5 receptor with internal deletion in hyperparathyroid tumors with implications for deregulated WNT/beta-catenin signaling. *PLoS Med.* **4**, e328 (2007).

34. Bjorklund, P., Svedlund, J., Olsson, A. K., Akerstrom, G. & Westin, G. The internally truncated LRP5 receptor presents a therapeutic target in breast cancer. *PLoS ONE* **4**, e4243 (2009).

35. Mao, J. et al. Low-density lipoprotein receptor-related protein-5 binds to axin and regulates the canonical Wnt signaling pathway. *Mol. Cell* **7**, 801–809 (2001).

36. Brennan, K., Gonzalez-Sancho, J. M., Castelo-Soccio, L. A., Howe, L. R. & Brown, A. M. C. Truncated mutants of the putative Wnt receptor LRP6/Arrow can stabilize β-catenin independently of Frizzled proteins. *Oncogene* **23**, 4873–4884 (2004).

37. Li, L. et al. REGgamma is critical for skin carcinogenesis by modulating the Wnt/beta-catenin pathway. *Nat. Commun.* **6**, 6875 (2015).

38. Tang, X. et al. UBQLN4 is activated by C/EBPbeta and exerts oncogenic effects on colorectal cancer via the Wnt/beta-catenin signaling pathway. *Cell Death Discov.* **7**, 398 (2021).

39. Wang, H. et al. Histone acetylation by HBO1 (KAT7) activates Wnt/beta-catenin signaling to promote leukemogenesis in B-cell acute lymphoblastic leukemia. *Cell Death Dis.* **14**, 498 (2023).

40. Hovanes, K. et al. β-catenin–sensitive isoforms of lymphoid enhancer factor-1 are selectively expressed in colon cancer. *Nat. Genet.* **28**, 53–57 (2001).

41. Li, T. W. H. et al. Wnt activation and alternative promoter repression of LEF1 in colon cancer. *Mol. Cell. Biol.* **26**, 5284–5299 (2006).

42. Atcha, F. A., Munguia, J. E., Li, T. W. H., Hovanes, K. & Waterman, M. L. A new β-catenin-dependent activation domain in T cell factor. *J. Biol. Chem.* **278**, 16169–16175 (2003).

43. Hennig, K. M. et al. WNT/β-catenin pathway and epigenetic mechanisms regulate the Pitt-Hopkins syndrome and schizophrenia risk gene TCF4. *Mol Neuropsychiatry* **3**, 53–71 (2017).

44. Feng, Y., Lee, N. & Fearon, E. R. TIP49 regulates beta-catenin-mediated neoplastic transformation and T-cell factor target gene induction via effects on chromatin remodeling. *Cancer Res.* **63**, 8726–8734 (2003).

45. Tan, M. et al. The antihelmintic drug pyrvinium pamoate targets aggressive breast cancer. *PLoS ONE* **8**, e71508 (2013).

46. Wiegering, A. et al. The impact of pyrvinium pamoate on colon cancer cell viability. *Int. J. Colorectal Dis.* **29**, 1189–1198 (2014).

47. Xu, F. et al. Anthelmintic pyrvinium pamoate blocks Wnt/β-catenin and induces apoptosis in multiple myeloma cells. *Oncol. Lett.* https://doi.org/10.3892/ol.2018.8006 (2018).

48. Zheng, L., Liu, Y. & Pan, J. Inhibitory effect of pyrvinium pamoate on uveal melanoma cells involves blocking of Wnt/β-catenin pathway. *Acta Biochim. Biophys. Sin.* **49**, 890–898 (2017).

49. Dattilo, R. et al. Pyrvinium pamoate induces death of triple-negative breast cancer stem–like cells and reduces metastases through effects on lipid anabolism. *Cancer Res.* **80**, 4087–4102 (2020).

50. Xu, L. et al. WNT pathway inhibitor pyrvinium pamoate inhibits the self-renewal and metastasis of breast cancer stem cells. *Int. J. Oncol.* **48**, 1175–1186 (2016).

51. Vranic, S. et al. Real-world survival outcomes in patients with locally advanced or metastatic NTRK fusion-positive solid tumors receiving standard-of-care therapies other than targeted TRK inhibitors. *PLos ONE* **17**, e0270571 (2022).

52. Tatake, R. J. et al. Establishment and characterization of four new squamous cell carcinoma cell lines derived from oral tumors. *J. Cancer Res. Clin. Oncol.* **116**, 179–186 (1990).

53. Mulherkar, R. et al. Establishment of a human squamous cell carcinoma cell line of the upper aero-digestive tract. *Cancer Lett.* **118**, 115–121 (1997).

54. Dhawan, V. V. et al. Apoptosis induction and anti-cancer activity of LeciPlex formulations. *Cell. Oncol.* **37**, 339–351 (2014).

55. Chandrani, P. et al. Integrated genomics approach to identify biologically relevant alterations in fewer samples. *BMC Genomics* **16**, 936 (2015).

56. Dharavath, B. et al. Role of miR-944/MMP10/AXL- axis in lymph node metastasis in tongue cancer. *Commun. Biol.* **6**, 57 (2023).

57. Iyer, M. K., Chinnaiyan, A. M. & Maher, C. A. ChimeraScan: a tool for identifying chimeric transcription in sequencing data. *Bioinformatics* **27**, 2903–2904 (2011).

58. Yoshihara, K. et al. The landscape and therapeutic relevance of cancer-associated transcript fusions. *Oncogene* **34**, 4845–4854 (2014).

59. Shugay, M., Ortiz de Mendíbil, I., Vizmanos, J. L. & Novo, F. J. Oncofuse: a computational framework for the prediction of the oncogenic potential of gene fusions. *Bioinformatics* **29**, 2539–2546 (2013).

60. Ye, J. et al. Primer-BLAST: A tool to design target-specific primers for polymerase chain reaction. *BMC Bioinformatics* https://doi.org/10.1186/1471-2105-13-134 (2012).

61. Desai, S. et al. Fusobacterium nucleatum is associated with inflammation and poor survival in early-stage HPV-negative tongue cancer. *NAR Cancer* https://doi.org/10.1093/narcan/zcac006 (2022).

62. Dobin, A. et al. STAR: ultrafast universal RNA-seq aligner. *Bioinformatics* **29**, 15–21 (2013).

63. Li, H. & Durbin, R. Fast and accurate short read alignment with Burrows–Wheeler transform. *Bioinformatics* **25**, 1754–1760 (2009).

64. Wala, J. A. et al. SvABA: genome-wide detection of structural variants and indels by local assembly. *Genome Res.* **28**, 581–591 (2018).

65. Frankish, A. et al. Gencode 2021. *Nucleic Acids Res.* **49**, D916–D923 (2021).

66. Chen, X. et al. Manta: rapid detection of structural variants and indels for germline and cancer sequencing applications. *Bioinformatics* **32**, 1220–1222 (2016).

67. Dimauro, I., Pearson, T., Caporossi, D. & Jackson, M. J. A simple protocol for the subcellular fractionation of skeletal muscle cells and tissue. *BMC Res. Notes* https://doi.org/10.1186/1756-0500-5-513 (2012).

68. Morgenstern, J. P. & Land, H. Advanced mammalian gene transfer: high titre retroviral vectors with multiple drug selection markers and a complementary helper-free packaging cell line. *Nucleic Acids Res.* **18**, 3587–3596 (1990).

69. Donze, O. RNA interference in mammalian cells using siRNAs synthesized with T7 RNA polymerase. *Nucleic Acids Res.* **30**, 46e–46e (2002).

70. Lai, M. B. et al. TSPAN12 is a Norrin co-receptor that amplifies frizzled4 ligand selectivity and signaling. *Cell Rep.* **19**, 2809–2822 (2017).

71. Nagy, Á., Munkácsy, G. & Győrffy, B. Pancancer survival analysis of cancer hallmark genes. *Sci. Rep.* https://doi.org/10.1038/s41598-021-84787-5 (2021).

Author contributions
B.D. and A.D. conceptualized the study and designed the experiments. B.D., A.B., A.C., A.P., S.D., A.n.C., R.T., and P.U. performed experiments. B.D., A.B., A.C., A.P., S.D., P.U., and A.D. performed data analysis. S.N. generated the reagents and provided clinical samples. B.D. and A.D. wrote the manuscript. All authors have read and approved the final manuscript.

Competing interests
The authors declare no competing interests.

Additional information
Supplementary information The online version contains supplementary material available at https://doi.org/10.1038/s41698-024-00555-4.

Correspondence and requests for materials should be addressed to Amit Dutt.

Reprints and permissions information is available at http://www.nature.com/reprints

Publisher's note Springer Nature remains neutral with regard to jurisdictional claims in published maps and institutional affiliations.

Role of *miR-944/MMP10/AXL*- axis in lymph node metastasis in tongue cancer

Bhasker Dharavath [1,2], Ashwin Butle[1], Ankita Pal[1], Sanket Desai[1,2], Pawan Upadhyay[1,2], Aishwarya Rane[1], Risha Khandelwal[1], Sujith Manavalan [1], Rahul Thorat[3], Kavita Sonawane[4], Richa Vaish[2,4], Poonam Gera[2,5], Munita Bal[2,6], Anil K. D'Cruz[4,7], Sudhir Nair [2,4✉] & Amit Dutt [1,2✉]

Occult lymph-node metastasis is a crucial predictor of tongue cancer mortality, with an unmet need to understand the underlying mechanism. Our immunohistochemical and real-time PCR analysis of 208 tongue tumors show overexpression of Matrix Metalloproteinase, MMP10, in 86% of node-positive tongue tumors ($n = 79$; $p < 0.00001$). Additionally, global profiling for non-coding RNAs associated with node-positive tumors reveals that of the 11 significantly de-regulated miRNAs, *miR-944* negatively regulates *MMP10* by targeting its 3'-UTR. We demonstrate that proliferation, migration, and invasion of tongue cancer cells are suppressed by *MMP10* knockdown or *miR-944* overexpression. Further, we show that depletion of *MMP10* prevents nodal metastases using an orthotopic tongue cancer mice model. In contrast, overexpression of *MMP10* leads to opposite effects upregulating epithelial-mesenchymal-transition, mediated by a tyrosine kinase gene, *AXL*, to promote nodal and distant metastasis in vivo. Strikingly, *AXL* expression is essential and sufficient to mediate the functional consequence of *MMP10* overexpression. Consistent with our findings, TCGA-HNSC data suggests overexpression of *MMP10* or *AXL* positively correlates with poor survival of the patients. In conclusion, our results establish that the *miR-944/MMP10/AXL*- axis underlies lymph node metastases with potential therapeutic intervention and prediction of nodal metastases in tongue cancer patients.

[1] Integrated Cancer Genomics Laboratory, Advanced Centre for Treatment, Research, and Education in Cancer, Kharghar, Navi Mumbai, Maharashtra 410210, India. [2] Homi Bhabha National Institute, Training School Complex, Anushakti Nagar, Mumbai, Maharashtra 400094, India. [3] Laboratory Animal Facility, Advanced Centre for Treatment, Research and Education in Cancer, Kharghar, Navi Mumbai, Maharashtra 410210, India. [4] Division of Head and Neck Oncology, Department of Surgical Oncology, Tata Memorial Hospital, Tata Memorial Centre, Parel, Mumbai 400012, India. [5] Tissue Biorepository, Advanced Centre for Treatment Research and Education in Cancer, Kharghar, Navi Mumbai, Maharashtra 410210, India. [6] Department of Pathology, Tata Memorial Hospital, Tata Memorial Centre, Parel, Mumbai 400012, India. [7] Apollo Cancer Center, Apollo Hospitals, CBD Belapur, Navi Mumbai 400614, India.
✉email: sudhirvr@gmail.com; adutt@actrec.gov.in

Oral cancer constitutes cancers of the mucosal surfaces of the lips, the floor of the mouth, oral tongue, buccal mucosa, lower and upper gingiva, hard palate, and retromolar trigone that are primarily associated with tobacco usage[1,2]. Among sub-sites, tongue cancer is the most predominant sub-site for intraoral cancer in developed countries with a varying incidence in developing countries[3]. An occult or subclinical metastasis to the lymph nodes close to the site of the primary tongue tumor— not detectable by imaging methods or physical examination— is associated with dismal prognosis in 27–40% of patients[4–6]. The single treatment modality of early stage oral cancer with a curative intent includes surgical resection of the primary tumor along with neck dissection with or without adjuvant therapy[7]. However, due to the presence of even a single cancer-positive lymph node, the loco-regional metastasis, as observed in one-third of oral cancer patients leads to a poor 5-year survival of below 50%[8].

The migration and invasion of cancer cells that underlie metastasis are driven by a plural set of intricate genotypic, phenotypic and micro-environmental processes. Proteins that are related to microvascular angiogenesis and lymphangiogenesis have been identified to promote regional lymph node metastases (LNM)[9]. A recent gene expression study, performed with advanced stage samples, reported the association of LNM to chromosomal instability and DNA repair defects[10]. We earlier reported significant upregulation of *Matrix Metalloproteinase-10 (MMP10)* in early stage tongue tumor samples associated with nodal metastases[11]. Overexpression of *MMP10* has been reported to promote invasion, metastasis and regulate stemness of cancer cells through activation of Wnt signaling pathway in head and neck, and ovarian cancer, and promote tumor progression by regulating angiogenic and apoptotic pathways in cervical cancer[12–14]. Studies have demonstrated that *MMP10* is required for transformed growth and invasion of non-small cell lung cancer cells in vitro[15], is induced in bronchioalveolar stem cells (BASCs) transformed by oncogenic *KRAS*[16], and promotes *KRAS*-mediated lung tumorigenesis in vivo[17]. Additionally, *MMP10* has been reported to promote pre-metastatic niche formation[18] and found to be upregulated in early stage esophageal cancer patients[19]. However, the role of *MMP10* remains unexplored in lymph node metastasis in early stage tongue cancer. Here, we validate that MMP10 overexpression in a cohort of 208 tongue tumor samples (including samples of sufficient quality from the N-zero clinical trial) is significantly correlated with nodal metastases. This study demonstrates that overexpression of *MMP10* is sufficient and essential to induce tumor growth and nodal metastasis in an orthotopic mouse model. We also show that *miR-944* negatively regulates *MMP10*, and AXL signaling pathway mediates phenotypes associated with *MMP10* overexpressing tongue cancer. Furthermore, ectopic expression of *miR-944* or knockdown of *AXL* suppresses *MMP10*-promoted proliferation, invasion, and migration of tongue cancer cells, indicating a therapeutic approach to target tongue cancer.

Results

We previously reported over-expression of *MMP10* and its association with nodal metastases in early tongue cancer patients[11]. In the current study, we validate MMP10 expression in a large cohort of tongue patient samples with nodal metastases and describe the mechanistic role of *miR944/MMP10/AXL-* axis in tongue cancer using in vitro biochemical and cell-based assays and in vivo orthotopic tongue tumor mouse model.

MMP10 is upregulated in tongue cancer patients with lymph node metastasis. To validate if MMP10 expression could stratify

tongue cancer patients likely to develop metastases, we performed immunohistochemistry (IHC) for MMP10 protein using 98 retrospectively collected clinical samples that were part of the phase-3 N-zero clinical trial (NCT00193765). On the basis of 500 patients with early stage (T1 and T2) oral cancer, the N-zero clinical trial compared the survival advantages of elective neck dissection (END) and therapeutic neck dissection (TND). The study established END as a standard of care for patients with early stage clinically nodal negative (T1, T2 and N0) oral cancer and showed its superiority in terms of overall and disease-free survival rates. The specificity of the MMP10 antibody was confirmed with the inclusion of primary antibody alone and secondary antibody alone negative controls (Supplementary Fig. 1a, b). MMP10 protein was mainly detected in the cytoplasm of tumor cells (Fig. 1d). IHC results suggest significant overexpression of MMP10 protein in tongue cancer patients with lymph node metastasis ($p = 0.0035$) (Fig. 1a, c and Supplementary Fig. 1c). Of note, an increased expression of MMP10 at the invasive fronts of the tumor was observed compared to the center of the tumor (Fig. 1d). Additionally, we screened for the expression of *MMP10* transcripts by real-time PCR across 110 tongue tumor samples. The data suggest overexpression of *MMP10* transcript in lymph node metastatic patient samples compared to the non-metastatic patient's group, ($p < 0.0001$) (Fig. 1b). In the clinical settings, given that both IHC and real-time PCR are routinely performed, our analysis suggests overexpression of MMP10 in 68/79 (86%) of patients with lymph
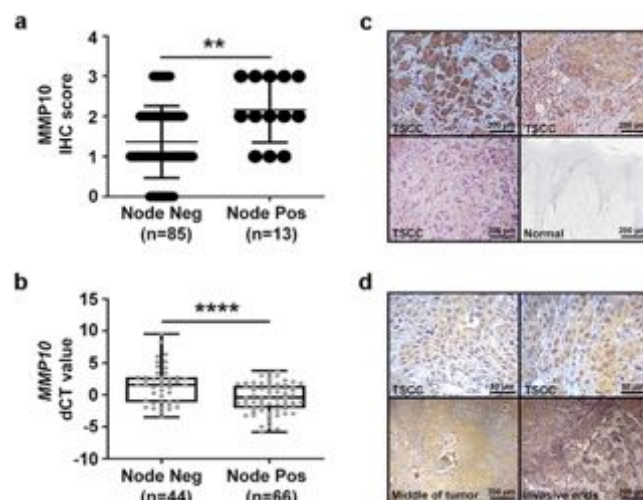

Fig. 1 MMP10 overexpression is associated with nodal metastasis in tongue cancer patients. a Immunohistochemistry of MMP10 in primary tongue tumor samples ($n = 98$). One dot represents IHC score of MMP10 in one sample. "Node Pos" and "Node Neg" represent primary tumor sample collected from patients with and without lymph node metastasis, respectively. Data are shown as means ± SD. **b** Quantitative real-time PCR (qRT-PCR) of *MMP10* transcript expression in primary tongue tumor samples ($n = 110$). *GAPDH* was used as reference control. Data is plotted as boxplot representation of delta Ct (dCT) values. The middle line in the boxplot shows median along with the lower (Q1) and upper quartiles (Q3) as boxes. The whiskers represent the minimum and maximum values. **c** Representative IHC stained photomicrographs of tongue tumors with scale bar (200 μm). The brown color indicates positive staining for MMP10 in tumor samples with different staining intensities (strong, moderate, weak). The normal epithelium is negative for MMP10. **d** Representative IHC stained images showing expression of MMP10 in cytoplasm of tumor cells (scale bar = 50 μm), in the middle region of tumor and at the invasive ends (scale bar = 200 μm). *p*-values are from Mann–Whitney tests and denoted as **$p < 0.01$; ****$p < 0.0001$. Data shown in (b) are representative of $n = 3$ independent replicates for each sample.

Table 1 Association of lymph node metastasis with *MMP10* expression in TCGA-tongue cancer data.

Samples	Nodal status	n (% along column)	MMP10 expression, n (% along row)		p-value
			Low expression	High expression	
TCGA-tongue cancer (n = 112)	Node positive	64 (57%)	44 (69%)	20 (31%)	0.0778
	Node negative	48 (43%)	40 (83%)	8 (17%)	
TCGA-early stage (T1-T2) tongue cancer (n = 62)	Node positive	31 (50%)	20 (65%)	11 (35%)	0.0816
	Node negative	31 (50%)	26 (84%)	5 (16%)	

node metastasis, whereas only 11/79 (14%) of patients with lymph node metastasis has low expression of MMP10 (chi-square value = 33.53, p-value < 0.00001). Specifically, real-time PCR and IHC data reveal MMP10 overexpression in 58/66 (88%) and 10/13 (77%), and low expression in 8/66 (12%) and 3/13 (23%) of patients with lymph node metastasis, respectively. Overall, of 208 tongue tumors we find MMP10 overexpression in 86% of node-positive tongue tumors (n = 79; p < 0.00001). The findings suggest MMP10 is strongly correlated with nodal metastases in tongue cancer. Next, we correlated MMP10 expression with clinical parameters including age, gender, smoking, alcohol consumption, and tobacco consumption. However, no significant correlation was found with any of the mentioned clinical parameters (Supplementary Table 1). Furthermore, we correlated *MMP10* transcript expression with nodal metastases in the TCGA-tongue cancer data of early stage as well as early and advanced stage samples. The samples in both the comparisons (early stage and all stages of tongue cancer) were divided into quartiles independently based on FPKM values of *MMP10* and the upper quartile of the samples were considered as the samples with high expression of *MMP10* and the rest of the three quartiles were considered as the samples with low expression of *MMP10*. Interestingly, we found a marginally significant correlation (p < 0.082) of *MMP10* transcript expression with lymph node metastasis in both analyses (Table 1). Overall, we observed significant upregulation of *MMP10* in tongue cancer patients with nodal metastasis, across 208 in-house and 112 TCGA tongue cancer samples.

MMP10 overexpression is essential and sufficient for cell proliferation, migration, and invasion of tongue cancer cells. To investigate the role of *MMP10* in metastasis of tongue cancer, we screened for MMP10 expression in three tongue cancer cell lines (AW13516, AW8507, and CAL27) by quantitative real-time PCR and Western blotting. AW8507 and CAL27 cell lines express higher levels of *MMP10* compared to AW13516 cells at both transcript and protein levels (Supplementary Fig. 2a–c). The AW13516 cell line was used for overexpression of *MMP10*, and AW8507 and CAL27 cell lines were used for knockdown of *MMP10*. Stable clones of AW13516 overexpressing *MMP10* cDNA were generated and confirmed for MMP10 overexpression by real-time PCR and Western blotting (Fig. 2a). To investigate the role of *MMP10* in metastasis, invasion and migration assays were performed. In vitro, wound-healing assay results suggested a significant increase in the migratory potential of AW13516 cells upon overexpression of *MMP10* as compared to the AW13516-vector control cells (Fig. 2b). Further, invasion assay also suggested a significant increase in the invasive potential of AW13516 upon overexpression of *MMP10* (Fig. 2c), suggesting sufficiency of *MMP10* overexpression to induce cellular migration. In a reciprocal approach, to study if *MMP10* expression is essential for the metastatic properties of tongue cancer cells, shRNA-mediated knockdown of *MMP10* was performed in AW8507 and CAL27 cells. *MMP10* was stably downregulated in both cell lines using three different shRNAs (sh-1, sh-2, and sh-3) and compared with non-targeting control shRNA (sh-NT). Knockdown of *MMP10*

was confirmed at transcript and protein level by real-time PCR and Western blotting assay, respectively (Fig. 2d, h). Cell proliferation assay performed with the clones suggested a significant decrease (p < 0.001) in the proliferation rate of cells upon knockdown of *MMP10* (Fig. 2e, i). To check if difference in proliferation rate is due to the difference in viability or proliferation or apoptosis. Using propidium iodide (PI) staining and flow cytometer-based sorting of live and dead cells, we conducted a cell viability study with shRNA-mediated *MMP10* knockdown clones of AW8507 and CAL27. Results did not show significant difference in the viability of cells upon *MMP10* knockdown (Supplementary Fig. 3a, e). The results were further supported by immunoblotting, which revealed comparable amounts of caspase 3 and PARP cleavage in the *MMP10* knockdown clones of AW8507 and CAL27 compared to control cells (Supplementary Fig. 3a, e). We performed siRNA-mediated knockdown of *MMP10* in AW8507 and CAL27 cells. The knockdown of *MMP10* was confirmed using real-time PCR (Supplementary Fig. 3b, f). Similar to viability assay, Annexin V-FITC/PI staining did not show significant difference in apoptosis of cells upon knockdown of *MMP10* (Supplementary Fig. 3c, d, g, h). These findings demonstrate that the difference in cell proliferation rates following *MMP10* knockdown is what causes the reduction in cell proliferation rates. Furthermore, depletion of *MMP10* in both the cell lines led to a significant decrease (p < 0.01) in the migratory and invasive potential of cells (Fig. 2f, g, j, k). Taken together, these results suggest that upregulation of *MMP10* is sufficient and essential to promote migration and invasion of tongue cancer cells.

Differentially expressed *miR-944* in primary tongue tumors targets 3'-UTR of *MMP10* to regulate lymph node metastasis. We performed an in silico analysis to investigate miRNAs predicted to bind to 3'-UTR of *MMP10* gene using 10 different miRNA binding site prediction tools, as described in the Methods section. The analysis identified 7 candidate miRNAs (*miR-944, miR-496, miR-152-3p, miR-130a, miR-148a, miR-148b*, and *miR-453-3p*) targeting the 3'-UTR of *MMP10* by at least 7 of 10 prediction algorithms (Supplementary Table 2 and Supplementary Fig. 4b). The 7 candidate miRNAs were validated by real-time PCR across 20 primary tongue tumors and paired adjacent normal samples derived from patients with nodal metastases (Supplementary Fig. 4e, 5). A Pearson's correlation analysis between the delta-delta CT values revealed a significant negative correlation between *MMP10* transcript and *miR-944* of the 7 candidate miRNAs (Supplementary Fig. 4d), downregulated in lymph node-positive tumors (Supplementary Fig. 4c). Interestingly, *miR-944* was also found to be significantly downregulated (fold change < 0.5 and p-value ≤ 0.05) in tumors with nodal metastases based on global miRNA profiling using Affymetrix miRNA 3.0 GeneChip constituting 5,778 unique mature human microRNAs probe sets (Supplementary Table 3 and Supplementary Fig. 4a).

To confirm biochemically whether *miR-944* directly targets the 3'-UTR of *MMP10*, 3'-UTR of *MMP10* gene was cloned downstream of the luciferase open reading frame (ORF) to construct a
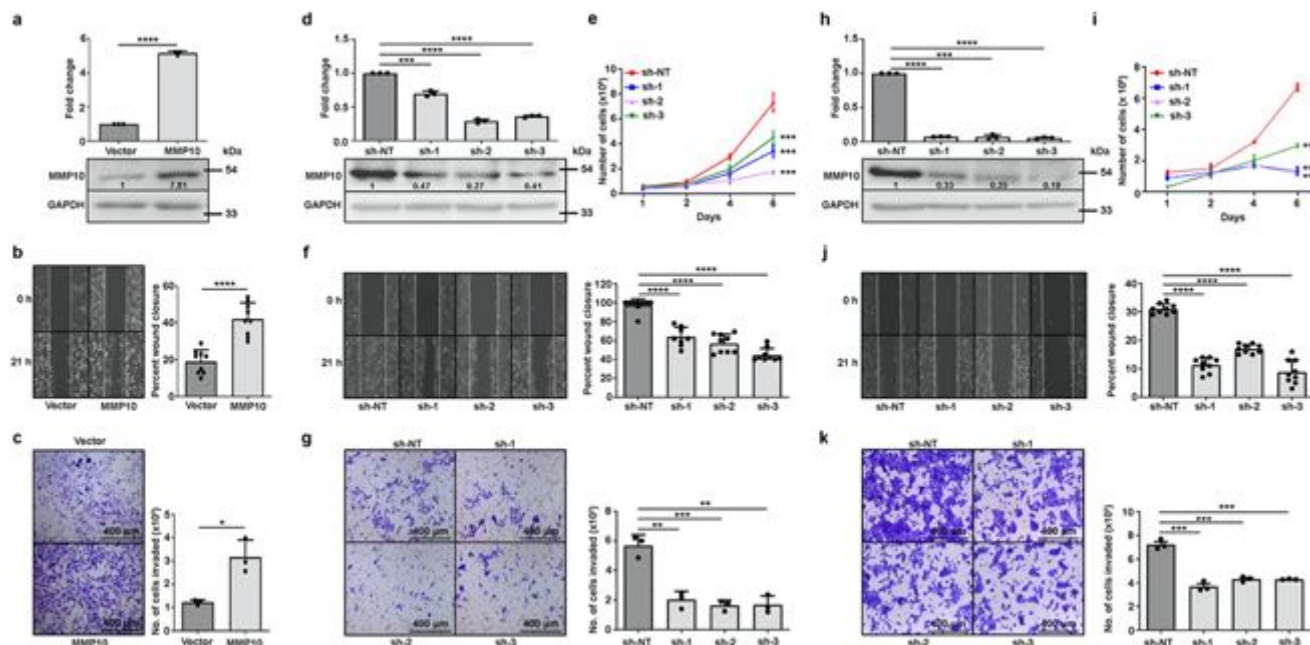
Fig. 2 Genetic perturbation of *MMP10* affects cell proliferation, migration and invasion of tongue cancer cells. a qRT-PCR and immunoblot of MMP10 and GAPDH in AW13516 cells stably overexpressing empty vector or *MMP10*. Numbers on the blot indicate intensity ratio of MMP10 expression with respect to the vector control lane. **b**, **f**, **j** Wound-healing assay of AW13516 cells stably overexpressing empty vector or *MMP10* (**b**), AW8507 cells (**f**) and CAL27 cells (**j**) with non-targeting shRNA (sh-NT) or stable *MMP10* knockdown (3 shRNAs – sh1 or sh-2 or sh-3). Representative images of wound-healing assay at 0 h and 21 h are presented along with the bar plots indicating the percentage of wound closure. **c**, **g**, **k** Boyden chamber matrigel invasion assay of AW13516 cells stably overexpressing empty vector or *MMP10* (**c**), AW8507 cells (**g**) and CAL27 cells (**k**) with sh-NT or stable *MMP10* knockdown with sh1 or sh-2 or sh-3. Representative images of crystal violet stained Boyden chamber along with the bar plots depict the percent cell invasion (scale bar = 400 μm). **d**, **h** qRT-PCR and immunoblot of MMP10 and GAPDH in AW8507 (**d**) and CAL27 (**h**) cells with sh-NT or stable *MMP10* knockdown. Numbers on the blot indicate intensity ratio of MMP10 expression with respect to the sh-NT control lane. **e**, **i** Cell proliferation assay of AW8507 (**e**) and CAL27 cells (**i**) with sh-NT or stable *MMP10* knockdown with sh-1 or sh-2 or sh-3. Scatter plots indicate the number of live cells on the mentioned day. Data are shown as means ± SD. *p*-values are from Student's unpaired *t*-test and denoted as *$p < 0.05$; **$p < 0.01$; ***$p < 0.001$; ****$p < 0.0001$. Data shown are representative of $n = 3$ independent experiments.

reporter plasmid pGL3-3'UTR-*MMP10* and *miR-944* was cloned in pcDNA-3.1(-) downstream to the CMV promoter. Transient co-transfection of 293FT cells with pc-DNA-*miR-944*, pGL3-3'UTR-*MMP10* reporter led to a significant decrease (*p*-value < 0.01, Unpaired student t-test) in the luciferase activity as compared to vector control, whereas a significant increase (*p*-value < 0.05, unpaired Student's *t*-test) in luciferase activity was observed post-co-transfection with anti-*miR-944* oligo (Fig. 3a). These results establish that the 3'UTR of *MMP10* is a target of *miR-944*.

Next, to understand the role of *miR-944* in metastasis of tongue cancer, *miR-944* was transiently overexpressed in AW8507 cells, which has endogenously low expression of the *miR-944* and high expression of *MMP10* (Supplementary Fig. 6). Overexpression of the miRNA was confirmed at the transcript level (Fig. 3b). Consistent with the results, overexpression of *miR-944* led to a significant downregulation (*p* < 0.01) in the expression of *MMP10* (Fig. 3c). Further, to assess the role of *miR-944* in tongue cancer, in-vitro cell-based assays were performed. A significant reduction in the proliferation rate (*p* < 0.01) of the cells was observed upon *miR-944* overexpression (Fig. 3d). Interestingly, migration and invasion assays suggested a significant decrease in the migratory and invasive phenotype (*p* < 0.001) of AW8507 cells upon *miR-944* overexpression (Fig. 3e, f). Taken together, these results reveal that *miR-944* is a negative regulator *MMP10* and suppresses the metastatic phenotype of tongue cancer cells upon its upregulation.

Consistent with the miRNA microarray study and biochemical findings, validation of *miR-944* expression in 63 tongue tumor samples suggested significant upregulation (*p* < 0.05) of *miR-944*

in patients with low expression of *MMP10* (based on the median expression) as compared to the patients with high expression of *MMP10* (Fig. 3g), suggesting downregulation of *MMP10* by *miR-944*. Furthermore, qRT-PCR based expression of *miR-944* across 93 tongue tumor patient samples suggests that *miR-944* is significantly downregulated (*p*-value < 0.05) in patients with nodal metastasis (Fig. 3h). Overall, we observed significant downregulation of *miR-944* and upregulation of *MMP10* in tongue cancer patients with nodal metastasis, suggesting that *miR-944/MMP10* is potentially involved in regulating lymph node metastasis.

MMP10 driven invasion and migration of tongue cancer cells is mediated by the AXL signaling pathway. Transcriptome sequencing was performed to investigate *MMP10* downstream targets involved in the regulation of tongue cancer metastasis. Differential expression analysis using cuffdiff and NOISeq tools revealed 110 statistically significant overlapping differentially expressed genes (−1.5 < log2FC > 1.5; *p*-value < 0.05 or prob > 0.95) in AW13516-*MMP10* overexpression clones compared to vector control cells (Supplementary Table 4). Of the 110 differentially expressed genes, 52 showed upregulation, and 58 showed down-regulation (Supplementary Fig. 7a). Analysis revealed significant upregulation (log2FC > 1.5; *p*-value < 0.05) of metastasis pathway-related genes (*AXL, CDH11, COL1A1, FGFBP1, IL6, IL7R, IL11,* and *MMP2*) upon ectopic overexpression of *MMP10* (Supplementary Fig. 7b and Supplementary Tables 4, 5). Along with metastasis pathway related genes, overexpression of *MMP10* also
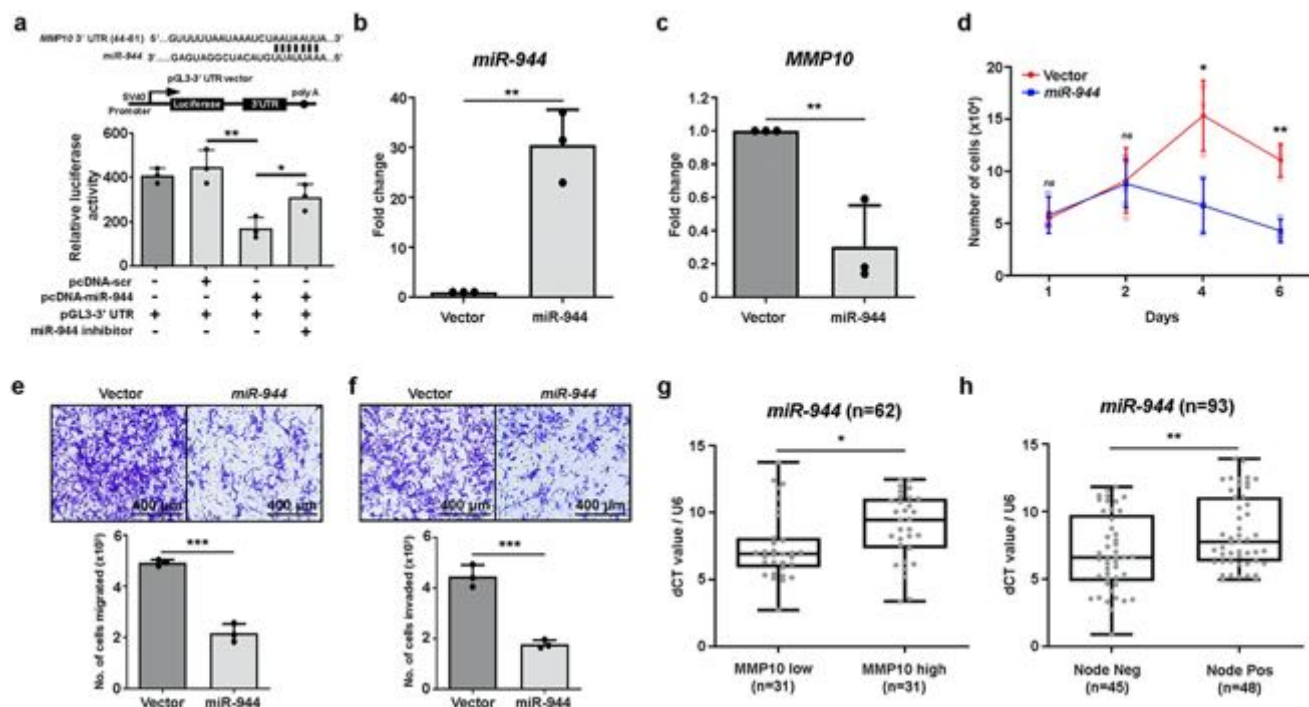
Fig. 3 *miR-944* targets *MMP10* to suppress metastasis in vitro and in tongue cancer patients. a Schematic diagram shows the *miR-944* target site on the 3'-UTR region of *MMP10* as predicted by TargetScan. Bar plot represents the relative luciferase activity measured by normalizing with the Renilla luciferase. **b, c** qRT-PCR of *miR-944* (**b**) and *MMP10* (**c**) expression in AW8507 cells overexpressing empty vector or *miR-944*. **d** Cell proliferation assay of AW8507 cells overexpressing empty vector or *miR-944*. Scatter plot indicate the number of live cells on the mentioned day. **e, f** Cell migration (**e**) and invasion assay (**f**) of AW8507 cells overexpressing empty vector or *miR-944* (scale bar = 400 μm). **g** qRT-PCR of *miR-944* mRNA in 62 primary tongue tumor samples correlated with *MMP10* mRNA expression. **h** qRT-PCR *miR-944* mRNA in 93 primary tongue tumor samples correlated with nodal metastasis status of patients. Data are plotted as boxplot representation of dCT values. *MMP10* and *miR-944* expression are normalized with *GAPDH* and *U6*, respectively. The middle line in the boxplot shows median along with the lower (Q1) and upper quartiles (Q3) as boxes. The whiskers represent the minimum and maximum values. Data are shown as means ± SD. *p*-values are from Student's unpaired *t*-test and denoted as *ns* (not significant); *$p < 0.05$; **$p < 0.01$; ***$p < 0.001$. Data shown are representative of $n = 3$ independent experiments.

upregulated EMT markers (*CDH2*, *SNAI2*, Vimentin, MMP9 and β-catenin), and downregulated MET marker (E-cadherin) which were validated in AW13516-*MMP10* overexpression clones using real-time PCR or immunoblotting (Supplementary Fig. 7c, d).

Next, we screened for the expression of metastasis pathway-related genes in 52 primary tongue tumors and correlated with *MMP10* expression. With the genes that significantly correlated ($p < 0.05$) with *MMP10* expression (*AXL, CDH11, FGFBP1, IL7R*, and *IL11*) (Supplementary Fig. 8), we performed Kaplan–Meier survival analysis using TCGA-HNSC data. Survival analysis suggests high expression of *MMP10* or *AXL* was significantly ($p < 0.05$) associated with poor overall survival of head and neck squamous cell carcinoma (HNSCC) patients (Supplementary Fig. 9), but not just tongue cancer patients, which could be because there were fewer tongue cancer patients. Also, multiple studies have reported that overexpression of *AXL* promotes metastasis in various cancers, including oral cancer[20,21]. We set to study the role of *AXL* in *MMP10*-promoted invasion and migration of tongue cancer. We screened for the expression of AXL transcript and protein in tongue cancer cell lines (Supplementary Fig. 10a, b). We asked if the knockdown of *MMP10* affects *AXL* expression in the cells ectopically overexpressing *MMP10*. We performed siRNA-mediated knockdown of *MMP10* in AW13516-*MMP10* overexpression clones and observed *AXL* to be significantly downregulated (Supplementary Fig. 11a, b), confirming that *MMP10* regulates *AXL* expression. Further, we screened for the expression of AXL downstream signaling molecules (AKT, mTOR and NF-κB p65) upon overexpression and knockdown of *MMP10*. Results suggest that

overexpression of *MMP10* upregulates *AXL* and activates downstream signaling pathway whereas stable knockdown of *MMP10* suppresses these effects (Fig. 4a). Furthermore, we investigated whether *AXL* overexpression in *MMP10* knockdown clones or *AXL* knockdown in *MMP10* overexpression clones would reverse the activation or inactivation of AXL downstream signaling, respectively. We performed stable overexpression of *AXL* in AW13516 (cell line with endogenously low levels of *MMP10*) and AW8507-*MMP10* knockdown cells, and siRNA-mediated knockdown of *AXL* in AW13516-*MMP10* overexpression clones. We found that overexpressing *AXL* activates AXL signaling in *MMP10* knockdown cells whereas knocking down *AXL* inactivates AXL signaling in *MMP10* overexpressing cells (Fig. 4b), indicating that AXL signaling is downstream of *MMP10*.

To study if *AXL* regulates *MMP10*-mediated proliferation, migration, and invasion of cells in the downstream, *AXL* overexpression and knockdown clones were used for in vitro metastasis-related cell-based assays. *AXL* knockdown significantly reduced the biochemical levels of p-AKT, p-mTOR and p-NF-κB p65 levels and impeded the *MMP10*-driven proliferation, migration, and invasion phenotypes, whereas *AXL* overexpression clones restored the p-AKT and p-NF-κB p65 levels along with proliferation, migration, and invasion phenotypes of *MMP10*-knocked down AW8507 cells (Fig. 4b–k), indicating that *AXL* is downstream of *MMP10* and could potentially regulate the ability of tongue cancer cell lines to metastases upon *MMP10* upregulation. Taken together, these findings indicate that *MMP10*-mediated migration and invasion of tongue cancer cells
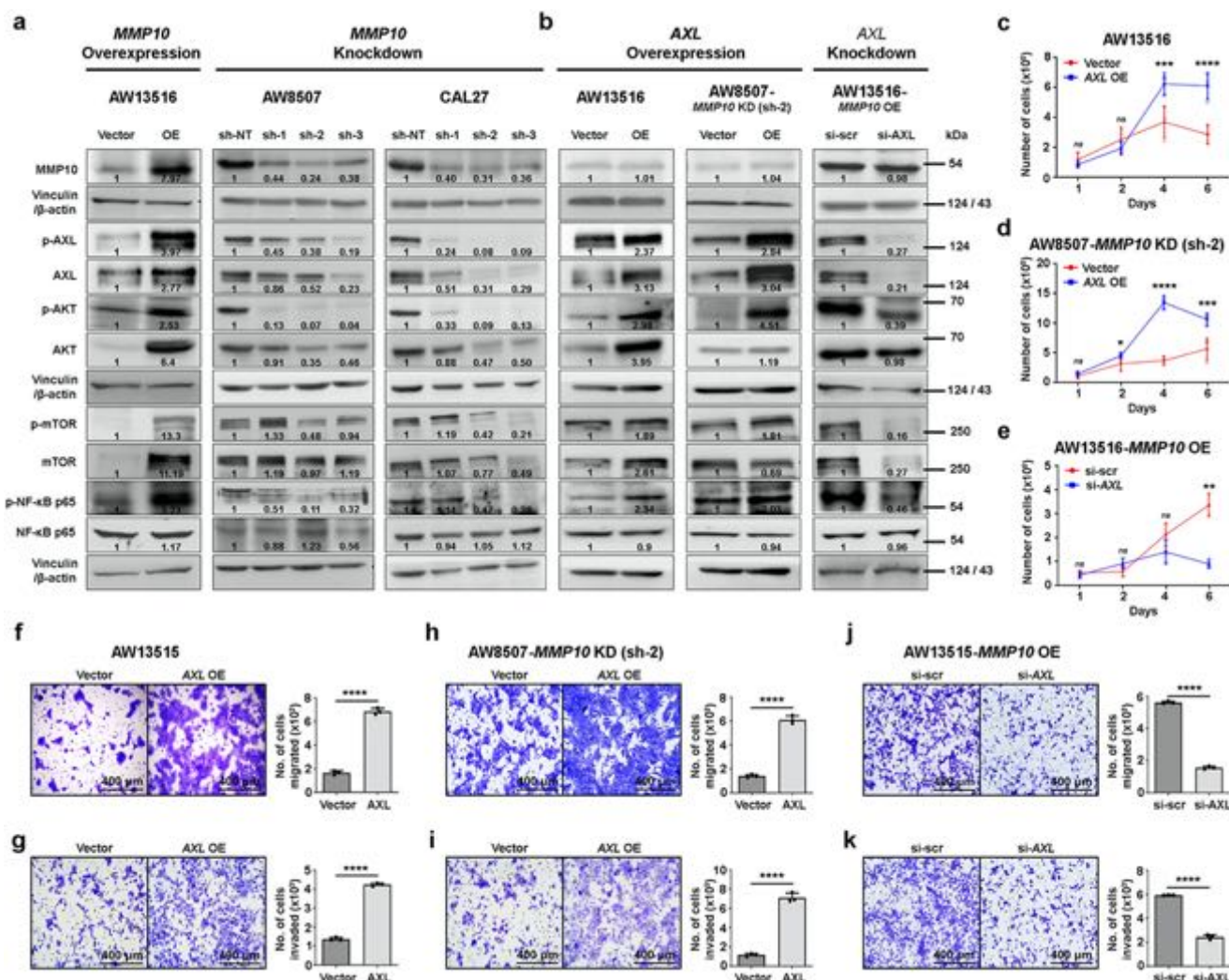
Fig. 4 miRNA-944/MMP10 induced EMT is mediated by the AXL signaling pathway. a, b Immunoblot of MMP10, p-AXL, AXL, p-AKT, AKT, p-mTOR, mTOR, p-NF-κB p65, NF-κB p65, Vinculin and β-actin upon overexpression/ knockdown of *MMP10* (**a**) or overexpression/ knockdown of *AXL* (**b**) in tongue cancer cell lines. Vinculin or β-actin was used as loading control. Numbers on the blot indicate intensity ratio of target protein expression with respect to the vector control lane. **c–e** Cell proliferation assay of AW13516 cells stably overexpressing empty vector or *AXL* (**c**), AW8507-*MMP10* knockdown cells stably overexpressing empty vector or *AXL* (**d**) and AW13516-*MMP10* overexpression cells with scrambled siRNA (si-scr) or siRNA-mediated knockdown of *AXL* (**e**). Scatter plots indicate the total number of live cells on the mentioned day. Boyden chamber migration (**f, h, j**) and invasion assays (**g, i, k**) of AW13516 cells stably overexpressing empty vector or *AXL* (**f, g**), AW8507-*MMP10* knockdown cells stably overexpressing empty vector or *AXL* (**h, i**) and AW13516-*MMP10* overexpression cells with scrambled siRNA or siRNA-mediated knockdown of *AXL* (**j, k**) plotted as bar plots indicating the percentage of cells migrated or invaded, respectively. Representative images of crystal violet stained Boyden chambers are shown (scale bar = 400 μm). Data are shown as means ± SD. *p*-values are from Student's unpaired *t*-test and denoted as *ns* (not significant); *$p < 0.05$; **$p < 0.01$; ***$p < 0.001$; ****$p < 0.0001$. Data shown are representative of $n = 3$ independent experiments.

is regulated by activation of the AXL signaling pathway and upregulation of EMT marker genes.

The orthotopic tongue tumor mouse model validates the role of *MMP10* in nodal metastasis. To confirm the in vitro findings and study the role of *MMP10* in tumorigenesis and metastasis of tongue cancer in vivo, we established orthotopic tongue tumor mouse model using the *MMP10* overexpression and knockdown clones. We injected luciferase-tagged AW13516 clones of *MMP10* overexpression, and CAL27 and AW8507 clones of *MMP10* knockdown (sh-2) along with vector control cells orthotopically into the tongue of 6 mice/group using needle gauge (30 G) after anesthetizing the mice with isoflurane. Caliper measurements at regular intervals showed that AW13516 cells form tumors after

25 days, CAL27 cells form tumors after 10 days, whereas, AW8507 cells formed tumors after 35 days of injection. However, the volume of AW8507-induced tumors was higher than CAL27-induced tumors, followed by AW13516-induced tumors. Interestingly, knockdown of *MMP10* significantly reduced the tumor volume in both AW8507-induced and CAL27-induced compared to the control group (Supplementary Figs. 12a, b), suggesting the role of *MMP10* in tumorigenesis of tongue cancer. Also, AW13516- and AW8507-induced tumors metastasized to cervical lymph nodes, lung, liver and kidney whereas, CAL27-induced tumors did not metastasize to any organ or lymph nodes (Supplementary Figs. 12c, 13a–c). Of note, the CAL27 cell line is reported to be a non-metastatic cell line in literature as well[22]. In AW13516-induced tumors, metastasis was observed in 6/6 (100%) mice in the *MMP10* overexpression group and 1/6
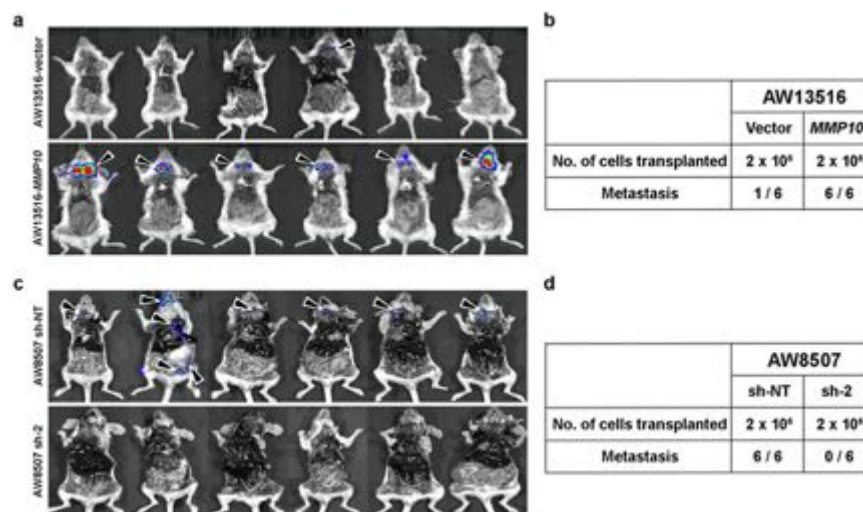
Fig. 5 MMP10 promotes metastases of tongue cancer in vivo. a, c IVIS imaging for detection of metastasis in mice injected ($n = 6$/group) with AW13516 cells stably overexpressing empty vector or *MMP10* (**a**) and AW8507 cells with sh-NT or *MMP10* knockdown (**c**). Bioluminescence imaging was performed after the resection of primary tongue tumors from the mice. The black arrowhead indicates the metastasis in regional lymph nodes and distant organs. **b, d** Tabular representation of the number of cells injected orthotopically into the tongue of mice and number of mice with metastasis in regional lymph nodes or distant organs.

(16.7%) in vector control group. In AW8507-induced tumors, metastasis was observed in 6/6 (100%) mice in the control group and none (0/6) in the *MMP10* knockdown group (Fig. 5a–d), suggesting a significant increase in the metastasis of tongue cancer upon overexpression of *MMP10* and decrease in metastasis upon depletion of *MMP10*. Overall, we demonstrate with the orthotopic tongue tumor mouse model that *MMP10* regulates tumorigenesis and metastasis of tongue cancer.

Discussion

The rate of occult lymph nodal metastasis of tongue cancer is between 20–30%[4]. There is an unmet need to understand the underlying mechanism to design an effective therapeutic strategy. Here, we present the molecular mechanism of *miR-944*/*MMP10*/*AXL*- axis mediated tongue cancer metastasis. Several lines of evidence suggest the pathway is essential and sufficient to induce nodal metastasis in tongue cancer patients.

Firstly, our immunohistochemical and real-time PCR-based analysis of MMP10 in 208 tongue tumor samples (including 98 N-zero clinical trial samples and 110 fresh-frozen samples) suggests a significant overexpression of MMP10 in primary tongue tumors of node-positive patients ($p < 0.00001$). The results show accurate prediction of nodal metastases in 86% (68 of 79) of node-positive patients based on MMP10 expression with 14% (11 of 79) false negative. While most patients with early stage tongue cancer receive elective neck dissection as standard therapy in India and other counties, testing for MMP10 expression may allow for the substantial majority of pathological node-negative individuals to avoid the invasive surgical operation associated with significant morbidity.

Secondly, ectopic overexpression or shRNA-mediated knockdown of *MMP10* affects cell proliferation, migration, and invasion of tongue cancer cells. These findings are consistent with previous reports where upregulation of *MMP10* has been shown to promote invasion and migration in several cancer types[12,14,23], including HNSCC[13]. Furthermore, as *MMP10* is reported to be upregulated in primary tumors of tongue cancer[11], we investigated for miRNAs predicted to be targeting *MMP10* and regulating its expression in tongue cancer. *In-silico* prediction of the

miRNA binding sites in 3'-UTR of *MMP10* revealed seven miRNAs potentially targeting *MMP10* and qRT-PCR based analysis of these miRNAs across 20 paired normal primary tongue tumors indicated *miR-944* as potential candidate miRNA showing highest negative correlation with *MMP10* transcript expression. Our study confirms *MMP10* as a direct target of *miR-944* by performing luciferase reporter assay in presence of *miR-944* and *miR-944* inhibitors. Moreover, we show that overexpression of *miR-944* downregulates *MMP10*, thereby, suppressing proliferation, migration, and invasion of tongue cancer cells. *miR-944* is reported to have both tumor suppressor[24] and oncogenic[25,26] potential in various cancer types. Our findings are consistent with previous reports where overexpression of *miR-944* has been shown to suppress the invasion and migration of cells[24,27].

Thirdly, in order to understand the downstream pathway mediating *MMP10*-promoted metastasis, we performed whole transcriptome sequencing of tongue cancer lines overexpressing *MMP10* followed by qRT-PCR based validation across 52 primary tongue tumor samples and identified upregulation of *AXL*, a receptor tyrosine kinase gene. The overexpression of *MMP10* also activated AXL downstream signaling molecules (AKT, mTOR, and NF-κB p65) and upregulated key EMT marker genes (*CDH2*, *SNAI2*, Vimentin, MMP9, and β-catenin) whereas, knockdown of *MMP10* suppressed AXL downstream signaling. Interestingly, knockdown of *AXL* suppresses *MMP10*-promoted proliferation, invasion, and migration of tongue cancer cells. And, over-expression of *AXL* promotes *MMP10*-suppressed proliferation, invasion, and migration of tongue cancer cells. These results are consistent with literature that suggests that overexpression of *AXL* promotes proliferation, migration and invasion whereas, genetic knockdown or pharmacological inhibition suppresses these phenotypes in various cancers[20,28,29], including HNSCC and oral cancer[30,31]. Thus, our findings indicate that *AXL* could be a potential therapeutic target in tongue cancer patients.

Fourthly, TCGA-HNSC data suggests poor overall survival of patients ($p < 0.05$) upon overexpression of *MMP10* or *AXL* expression positively correlates with expression of *MMP10* and poor overall survival of the patients, as shown in various cancer types[32,33], including oral cancer[31]. Interestingly, *miR-944* expression is significantly negatively correlated with *MMP10* expression
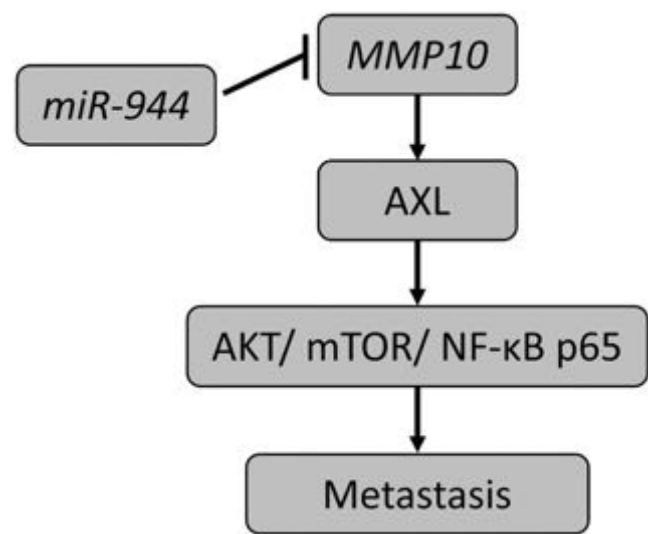
Fig. 6 Model depicting *miR-944/MMP10/AXL-* axis to regulate metastasis in tongue cancer. The working model demonstrating the role of *MMP10* in promoting metastasis via activation of AXL signaling pathway and is negatively regulated by *miR-944* in tongue cancer.

($p < 0.05$) and lymph node metastasis ($p < 0.01$), suggesting a significant role of the *miR-944/MMP10/AXL-* axis.

Lastly, we validate our in vitro findings establishing the role of *MMP10* in tongue cancer metastasis using an orthotopic tongue tumor mouse model. We present that overexpression of *MMP10* promotes metastasis (16.7% in WT cells versus 100% in *MMP10* overexpressing cells) and suppression of *MMP10* reduces tumor volume as well as metastasis (100% in WT cells versus 0% in *MMP10* knocked down cells) of tongue cancer in orthotopic tongue tumor mouse model. Although *MMP10* is primarily known for promoting metastatic potential of the tumor cells[13,33], literature also suggests a role of *MMP10* in tumor initiation and progression[12,14]. In cervical and ovarian cancer, *MMP10* is known to be involved in tumorigenesis and metastasis[12,14].

Taken together, our findings describe the role of *miR-944/ MMP10/AXL-* axis in lymph node metastasis in tongue cancer (model summarizing the axis is depicted in Fig. 6). Targeting *AXL* may represent a novel therapeutic approach in managing tongue cancer patients. Additionally, previous studies to stratify the patients likely to develop nodal metastases–not detectable by imaging methods or physical examination, have documented diagnostic limitations. Its reduction could eliminate misdiagnosis sparing 70 to 80% of the patients from morbid elective neck dissection. Thus, low expression of *miR-944* or overexpression of MMP10 as a prognostic biomarker could also help predict nodal metastasis in tongue cancer, an assessment that awaits designing a larger prospective randomized clinical trial.

Methods

Patient sample details. A total of 130 fresh frozen tongue tumor samples were used to screen for the expression of *MMP10* and *miR-944* by quantitative real-time PCR and an additional set of all available 98 formalin-fixed paraffin-embedded (FFPE) tissue blocks with adequate tumor content and quality, as a part of the N-zero clinical trial, were used for screening of MMP10 protein expression by immunohistochemistry. Primary tongue tumors were staged as T1 (measuring ≤2 cm) or T2 (measuring >2 cm but <4 cm) as per AJCC (American Joint Committee on Cancer)/UICC (Union for International Cancer Control) TNM classification system (8th edition). Patients were classified as N0 (node-negative) or N1 (node-positive) status based on the final histopathology report of the primary tumor. Patient sample details are provided in Table 2. The patient details include age, gender, anatomic site, TNM tumor stage, nodal status, smoking (represents the patients with habits of smoking tobacco as cigarettes, cigars or pipes), chewing, alcohol, tobacco (represents the patients with the habit of smoke-less tobacco chewing), recurrence, metastasis and status at last follow-up (the last follow-up date of patients ranges from 1 month to 11.9 years with a median follow-up of 3.8 years. As the patient samples were collected retrospectively, the follow-up period was not reached to 5-year mark in all patients).

Ethical approval. All the patient samples were collected from the tumor tissue repository of Tata Memorial Hospital (TMH-TTR) and the Advanced Centre for Treatment, Research and Education in Cancer (ACTREC-TTR), Mumbai. Samples were collected with the approval of The Institutional Review Board (IRB) and the Ethics Committee (EC) of Tata Memorial Centre-ACTREC. Since the samples were collected retrospectively, the IRB and EC waived the need for informed consent.

Cell culture. AW13516 and AW8507 tongue cancer cell lines were obtained from Tata Memorial Hospital while CAL27 cells were procured from ATCC. Cells were tested for mycoplasma and were made mycoplasma-free using the EZKill mycoplasma removal reagent (Cat No. CCK006-1, HiMedia). The cell lines were authenticated by DNA short tandem repeat (STR) profiling using Promega Geneprint 10 system in conjugation with GeneMarker HID software tool. All the cell lines (AW13516, AW8507 and CAL27) were cultured in Dulbecco's Modified Eagle Medium (Cat No. 12800-017, Gibco) at 37 °C in a 5% CO_2 incubator. Culture media was supplemented with 10% fetal bovine serum (FBS) (Cat No. 10270106, Gibco) and 1.25 µL/mL gentamycin (Abbott). Trypsinization was performed using 0.25% Trypsin-EDTA (Cat No. TC245, HiMedia) and cells were suspended in 90% FBS and 10% DMSO (Cat No. D5879, Sigma-Aldrich) freezing mix for long term storage in liquid Nitrogen.

Tissue processing, RNA extraction, and real-time PCR. RNA extraction from the tissue samples was performed using AllPrep DNA/RNA/miRNA Universal Kit (Cat No. 80224, QIAGEN). About 20–30 mg tissue sections were cut into small pieces and subjected to bead-based homogenization in 600 µL lysis buffer using

Table 2 Clinical characteristics of 228 patients in the study.		
Clinicopathological features	**Variable**	**Frequency ($n = 228$), n (%)**
Age	Median (range)	46 (23-76)
	<40	61 (27%)
	40–60	125 (55%)
	>60	32 (14%)
	NA	10 (4%)
Gender	Male	165 (73%)
	Female	53 (23%)
	NA	10 (4%)
Anatomic site	Oral Tongue	228 (100%)
TNM Tumor stage	pT1-T2	167 (73%)
	pT3-T4	61 (27%)
Nodal Status	Node positive	83 (36%)
	Node negative	145 (64%)
Smoking	Smoker	53 (23%)
	Non-smoker	165 (73%)
	NA	10 (4%)
Chewing	Chewer	119 (53%)
	Non-chewer	99 (43%)
	NA	10 (4%)
Alcohol	Yes	43 (19%)
	No	175 (77%)
	NA	10 (4%)
Tobacco	Yes	135 (60%)
	No	83 (36%)
	NA	10 (4%)
Recurrence	Yes	116 (51%)
	No	102 (45%)
	NA	10 (4%)
Metastasis	Yes	49 (21%)
	No	169 (75%)
	NA	10 (4%)
Status at last follow-up	Alive	169 (75%)
	Died	49 (21%)
	NA	10 (4%)

NA = Information not available.

FastPrep homogenizer (MP Biomedicals, USA) and further processed for total RNA extraction as per manufacturer's protocol. Total RNA was extracted from the cell lines using TRIzol reagent (Cat No. T9424, Sigma-Aldrich) based method. Total RNA obtained from tissue samples and cell lines were further subjected to DNase treatment using DNA-free Kit (Cat No. AM1906, Ambion) for removal of the residual genomic DNA. RNA concentration was measured using NanoDrop 2000c Spectrophotometer (ThermoFisher Scientific). First-strand cDNA synthesis was performed using PrimeScript TM 1st strand cDNA synthesis kit (Cat No. RR370A, TaKaRa) as per the manufacturer's protocol. Quantitative real-time PCR was performed using KAPA SYBR real-time PCR master mix (Cat No. KK4601, Sigma-Aldrich) on QuantStudio 12 K Flex Real-Time PCR System (Cat No. 4470935, Applied Biosystems). For quantitative real time PCR of each sample, 6 µL reaction in triplicates were incubated in a 384-well plate at 95 °C for 5 min, followed by 40 cycles of 95 °C for 15 s, 64 °C for 15 s, and 72 °C for 15 s. Primer sequences used for real-time PCR validation of genes are provided in Supplementary Table 6. All real-time PCR experiments were performed in triplicates for each of the three experimental replicates. For real-time PCR analysis, delta-CT (dCt) values were calculated, and samples were sorted into quartiles based on delta-CT values. Samples in the lower quartile were considered as the samples with low expression of *MMP10* and the top three quartiles of the samples were considered as the samples with high expression of *MMP10*.

Protein sample preparation and western blotting. Cells were grown to 70–80% confluence in a 10 cm culture dish and washed thoroughly with sterile 1X PBS. The cells were harvested using a sterile cell scraper, and cell lysates were prepared in RIPA Buffer (Cat No. R0278, Sigma-Aldrich) along with a protease inhibitor cocktail (Cat No. P8340, Sigma-Aldrich) and 0.1 M DTT. After intermittently tapping and vortexing the samples on ice for 30 min, cell debris was pelleted by centrifugation at 14000 rpm for 40 min and the supernatant was collected. Protein concentrations were estimated using BCA reagent (Cat No. MP152414, MP Biomedicals). Bovine serum albumin (Cat No. 0216006980, MP Biomedicals) was used as a standard and estimations for each sample was performed in triplicate. For Western blotting, 50 µg of protein was loaded on 10% SDS-PAGE and transferred to PVDF membrane (Cat No. 10600021, Amersham Hybond, GE healthcare) using a wet transfer method. PVDF membrane blocking was performed using 5% BSA to avoid nonspecific binding of antibody. Primary antibodies were diluted in 3% BSA solution prepared in 1X TBST and incubated overnight at 4 °C. Primary antibodies for MMP10 (Cat No. MAB910, Bi Biotech; dilution 1:1000), GAPDH (sc-32233, Santa Cruz Biotechnology; dilution 1:2000), phospho-AXL (DY702, CST; dilution 1:1000), AXL (C89E7, CST; dilution 1:1000), phospho-AKT (4060 T, CST; dilution 1:100), AKT (4685 S, CST; dilution 1:500), Vinculin (4650 S, CST; dilution 1:1000), β-actin (sc-47778, Santa Cruz Biotechnology; dilution 1:2000), phospho-mTOR (5536 T, CST; dilution 1:1000), mTOR (2983 T, CST; dilution 1:1000), phospho-NF-κB p65 (3033 T, CST; dilution 1:2000), NF-κB p65 (ab16502, abcam; dilution 1:2000), Caspase 3 (9662 S, CST; dilution 1:1000), PARP (9542 S, CST; dilution 1:2000), α-Tubulin (T5168, Sigma-Aldrich, 1:2000), E-cadherin (3195 T, CST; dilution 1:2000), Vimentin (5741 T, CST; dilution 1:2000), MMP9 (13667 T, CST; dilution 1:500) and β-catenin (ab32572, abcam; dilution 1:2000) were used for Western blotting. Goat anti-rabbit IgG-HRP secondary antibody (sc-2004, Santa Cruz Biotechnology; dilution 1:2000) was used for the detection of phospho-AXL, AXL, phospho-AKT, AKT, Vinculin, phospho-mTOR, mTOR, phospho-NF-κB p65, NF-κB p65, Caspase 3, PARP, α-Tubulin, E-cadherin, Vimentin, MMP9 and β-catenin. Goat anti-mouse IgG-HRP secondary antibody (sc-2005, Santa Cruz Biotechnology; dilution 1:2000) was used for the detection of MMP10, GAPDH and β-actin. ECL Western Blotting Substrate (Cat No.T7101A, TAKARA) was used for visualization of the luminescence on the Chemidoc system (Bio-Rad). Western blot protein intensities were normalized and quantified using ImageJ software. TIFF files of western blot images were used for quantification. Using the rectangular tool in ImageJ, protein band intensity was measured and normalized with the background intensity in same blot to obtain the normalized band intensity. The actual band intensities were obtained by further normalization with the reference loading control. Fold change expression of each protein was obtained by comparing the actual band intensity of the protein in the overexpression/ knockdown group versus vector control group. All the western blots were performed in three experimental replicates.

***MMP10*-miRNA target prediction and Luciferase assay**. The miRNAs targeting *MMP10*-3' UTR were predicted using the following databases and web servers: MirWalk[34], miRanda[35], mirbridge[36], miRDB[37], miRMap[38], miRNAMap[39], PicTar2[40], PITA[41], RNAhybrid[42] and Targetscan[43]. The primer sequences of miRNAs used for real-time PCR validation are provided in Supplementary Table 6. Real-time PCR data analysis was performed using the $2^{-\Delta\Delta Ct}$ method and *U6* was used as internal reference control. For luciferase assay, 293FT cells (50,000 cells/ well) were seeded in a 24 well plate, 12 h prior to transfection. The transfection was performed using lipofectamine 3000 reagent (Life Technologies, USA) with a combination of *miR-944* constructs, along with Renilla luciferase vector (for normalizing transfection efficiency) and 15 pmol mirVana miRNA-inhibitor (Ambion, USA) per well. The cells were lysed post 48 h of transfection and luciferase assay was performed to measure luminescence using a luminometer (Berthold Luminometer, Germany). The data were plotted as the ratio of

luminescence of firefly rennila luciferase. The experiment was performed in three replicates, and p-value < 0.05 (calculated using unpaired Student's t-test) was considered significant.

Cloning of *MMP10* cDNA, *MMP10*-3'UTR and *miR-944*. cDNA of human *MMP10* was amplified from CAL27 cell line using KAPA Taq DNA polymerase (Cat No. KK1024, Sigma-Aldrich) and cloned in pTZ57R/T cloning vector (InsTAclone PCR cloning kit, Cat No. K1214R, ThermoFisher Scientific) as per manufacturer's protocol. Full-length *MMP10* cDNA sequence was confirmed by Sanger sequencing and was sub-cloned into a retroviral expression vector, pBABE-puro (Addgene plasmid # 1764)[44], using restriction digestion based cloning with BamHI-HF (Cat No. R3136, NEB) and EcoRI (Cat No. ER0271, Fermentas) restriction enzyme sites. Similarly, complete *MMP10*-3'UTR was amplified by designing the primers flanking the 3'UTR with XbaI site for cloning in pGL3-promoter vector (Luciferase Expressing vector, Promega) at XbaI site. Sequencing of the construct was done to ensure the absence of any mutation. For cloning of *miR-944*, primers were designed to amplify the 432 bp flanking the *miR-944* seed sequence from the genomic DNA. The amplicon was sequence verified for mutations using Sanger sequencing and cloned in a pTZ57R/T vector (Fermentas, USA) followed by subcloning in pcDNA 3.1 (-) (ThermoFisher Scientific) using BamHI and HindIII restriction enzyme sites. The primers used for cloning are provided in Supplementary Table 7.

Transcriptome sequencing and data analysis. Transcriptome sequencing libraries were constructed by using the TruSeq RNA library protocol (Illumina). Briefly, mRNA was purified from 4 µg of intact total RNA using oligodT beads, and library preparation was done as per the manufacturer's instructions (TruSeq RNA Sample Preparation Kit, Illumina). Transcriptome sequencing was performed and generated at least 43 million reads per sample. Transcriptome sequencing data analysis was performed using the Tuxedo-suite pipeline[45]. In brief, alignment of short reads was done against the reference genome (GRCh38) using TopHat2 in which 95% of reads were mapped to the reference genome. Cufflinks v.2.0.2 was used to find the expressed transcripts in the data and cuffdiff was used for the identification of differentially expressed genes. Also, NOISeq[46] was used for differential expression analysis and overlapping genes were prioritized for functional experiments. Differentially expressed genes were used for the identification of enriched or depleted pathways by Reactome pathway analysis tool[47].

miRNA microarray analysis. Microarray-based global miRNA expression profiling of 5 primary tongue tumors derived from patients with no regional lymph node metastases (pT2N0); 4 primary tumors from patients with single lymph node metastasis (pT2N1); and, six adjacent tongue normal samples were analyzed using Affymetrix GeneChip miRNA 3.0 array (Affymetrix, Santa Clara, CA, USA). A 200 ng of total RNA was labeled with biotin using 3DNA Array Detection Flash-Tag™ Biotin HSR kit (Genisphere, Hatfield, PA, U.S.) as per manufacturer's instructions and subsequent hybridization for 16 h at 60RPM. The GeneChip® miRNA 3.0 array contained 25,146 probe sets including 5,639 human miRNAs probe set consisting of mature miRNAs, pre-miRNAs, snoRNAs, scaRNAs, and hypothetical miRNAs. The chip was washed and stained using Gene Chip Hybridization Wash and Stain Kit (Affymetrix) and was then scanned with the Affymetrix GeneChip Scanner 3000 7 G (Affymetrix, Santa Clara, CA, U.S.). All raw microarray data (.cel files) were pre-processed using RMA method[48] which includes background correction, log transformation, quantile normalization followed by essential quality control steps. Probe-centric data were converted into miRNA-centric data using an average over-replicate approach. We excluded snoRNA, hypothetical miRNA, control probes from the analysis and restricted analysis only for annotated microRNAs (miRBase-20 release), and the data was analyzed using BRB-ArrayTools developed by Dr. Richard Simon and the BRB-ArrayTools Development Team. Briefly, non-variable miRNAs were excluded from the analysis based on the log expression variation filter (variance of miRNAs across the arrays). The microRNAs were considered as differentially regulated if miRNA followed 0.5 < fold change > 1.5 filters along with p-value < 0.05. Class comparison analysis was carried out between tumors with node-positive status versus tumors with node-negative status. Class comparison results were plotted as a heatmap in MultiExperimentViewer (MeV version 4.9).

siRNA synthesis by in vitro transcription. Sense and anti-sense DNA oligonucleotides for *AXL* and *MMP10* (shown in Supplementary Table 8) were ordered from Sigma-Aldrich. The protocol for oligonucleotide-directed production of small RNA transcripts with T7 RNA polymerase is reported in the literature[49]. For each in vitro transcription (IVT) reaction, 1 nmol of each oligonucleotide (re-suspended in 1X TE buffer (10 mM Tris-HCl pH 8.0 and 1 mM EDTA)) was annealed using thermocycler to obtain double-stranded DNA (dsDNA). The thermocycler conditions used were: 95 °C for 3 min, followed by 70 cycles of 95 °C for 30 s (−1 °C/ cycle). In vitro transcription (IVT) reaction was performed in 20 µL of a reaction containing 1X T7 transcription buffer (Cat No. P118B, Promega), 1X biotin RNA labeling mix (Cat No. 11685597910, Sigma-Aldrich), 1 U RiboLock RNase Inhibitor (Cat No. EO0381, Fermentas), 10 U T7 RNA polymerase (Cat No. P2075, Promega) and 1 nmol of dsDNA, as a template. The reaction was incubated at

37 °C for 2 h. Sense and anti-sense siRNAs synthesized in separate reactions were annealed by mixing the transcription reactions at 95 °C for 1 min, followed by 70 cycles of 95 °C for 30 s (−1 °C/cycle) to obtain double-stranded small interfering RNA (siRNA).

Overexpression and knockdown studies. For overexpression of *MMP10* in the AW13516 cell line, the pBABEpuro-*MMP10* construct was used. Cells with pBABE-puro empty vector were used as a control for overexpression. For knockdown of *MMP10* in CAL27 and AW8507 cell lines, 3 lentiviral shRNA constructs (Transomic Technologies) were used. The short hairpin non-targeting (sh-NT) construct was used as vector control. Transfection was carried out using a lipofectamine kit (Cat No. L3000015, Invitrogen). Positive clones were selected using 0.5 µg/mL of puromycin (Cat No.TC198, Himedia). For stable verification of Myristoylated *AXL* in AW13516 and AW8507-*MMP10* knockdown (sh-2) cells, pWZL-Neo-Myr-Flag-*AXL* construct[50] was used. The construct was obtained as a kind gift from Dr. Shaida Andrabi (University of Kashmir, Jammu and Kashmir, India). Positive clones were selected using 1 mg/mL of G418 (Cat No. TC025, HiMedia). Transient siRNA-mediated knockdown of *MMP10* or *AXL* was performed with two siRNAs, targeting each gene, synthesized using T7 RNA polymerase. Following siRNA transfection for 48 h using Lipofectamine RNAiMAX (Cat No. 13778075, Invitrogen), cells were used for RNA isolation and in vitro cell-based assays. Transient overexpression of *miR-944*-pcDNA 3.1(-) was carried out in AW8507 cells. Transient transfection was performed by using lipofectamine (Cat No. L3000015, Invitrogen) and cells were collected after 48 h for RNA isolation and to perform cell-based assays. All the transient knockdown and overexpression experiments were performed in three independent replicates and the expression of target gene was screened before performing the cell based assays.

Cell Proliferation assay. Cell proliferation assay was performed in 24 well plates with a cell density of 10,000 cells/well for all the experiments. Cell growth was assessed at days 1, 2, 4, and 6 by passaging and counting viable cells by trypan blue staining and using a hemocytometer. All experiments were performed three times with each experiment performed in triplicates.

Wound-healing assay. An equal number of cells were seeded in 6-well tissue culture plate (3 wells per each clone) for control and overexpression or knockdown clones and cultured till the plate was confluent. Confluent monolayers in the plate were subjected to scratch (3 scratches for well) with a sterile pipette tip. Further, cells were washed with 1X PBS to remove debris and subsequently incubated with DMEM medium containing 10% FBS. Cell migration at the wound surface (3 wound per well with 3 wells per each clone = 9 wounds for each clone in one experiment) was imaged for a period of 21 h under an inverted microscope with one image at every 30 min. The quantification of cell migration was performed using the ImageJ wound healing plugin tool by measuring the distance of the wound edge of the migrating cells from the start point to the migrated point in nine separate wounds per each clone in one experiment. All the experiments were independently performed three times.

Boyden chamber invasion and migration assay. Boyden chamber matrigel invasion assay was performed using 24-well transwell inserts (Cat No. 353097, Corning) coated with 100 µg matrigel (Cat No. 354234, Corning) and allowed to settle for 16 h at 37 °C in 5% CO$_2$ incubator. Invasion assay was performed with 1×10^5 cells of AW8507-*MMP10* knockdown clones, 5×10^5 cells of CAL27-*MMP10* knockdown clones, 2×10^5 cells of *AXL* overexpression or knockdown clones and 4×10^5 cells of *miR-944* overexpression clones suspended in 300 µL serum-free medium and seeded in the Boyden chamber and 700 µL of 10% serum-containing DMEM medium was added in the companion plate wells. For migration assay, cells were seeded directly in the Boyden chamber without matrigel. For migration assay, 1×10^5 cells of *AXL* overexpression or knockdown clones and 2×10^5 cells of *miR-944* overexpression clones were used. The cells were allowed to invade/migrate for 48 h at 37 °C in 5% CO$_2$ incubator. The transwell chambers were fixed and stained with 0.1% crystal violet. After mounting the membrane using DPX mountant (Cat No. 18404, Qualigens) on a slide, invaded cells were imaged under an upright microscope at 10X magnification. Images of 10 random fields were chosen and the number of cells in each field were counted using the ImageJ cell counter plugin tool and plotted as percent cell invasion or percent cell migration. All the experiments were independently repeated three times with 2 inserts/clone in each experiment (total of 6 replicates per each clone).

Apoptosis assay. Apoptosis was measured by double-labeling the cells with Annexin V-fluorescein isothiocyanate (FITC) and propidium iodide using FITC Annexin V Apoptosis Detection Kit, as per the manufacturer's instructions (Cat No. 556570, BD Pharmingen). Briefly, 0.3 million cells of AW8507- and CAL27-*MMP10* knockdown along with scrambled control cells were re-suspended in 100 µL 1X Annexin V binding buffer and incubated on ice with 2 µL Annexin V-FITC conjugate for 15 min. This suspension was diluted to a final volume of 300 µL using ice-cold 1X Annexin V binding buffer and acquired immediately on Attune NxT Acoustic Focusing Cytometer (Life Technologies, ThermoFisher Scientific) after addition of 1 µL of 100 µg/mL Propidium iodide (PI). Data analysis

was performed using FlowJo software (v10.6.1). All the experiments including siRNA-mediated knockdown of *MMP10* in both cell lines were performed three times.

Cell viability assay. Cell viability was assessed by resuspension of 0.3 million cells in 300 µL 1X Annexin V binding buffer and addition of 1 µL of 100 µg/mL Propidium iodide (PI). Percent viable and late apoptotic/necrotic cells were acquired on Attune NxT Acoustic Focusing Cytometer. Data analysis was performed using FlowJo software. All the experiments were performed in three replicates.

Immunohistochemistry. Samples used for IHC were duly verified by two independent reviewers for histological examinations such as normal sample verification and percent tumor nuclei. The tumor sample with concordant histopathological diagnosis by both reviewers was included in the study. Immunohistochemistry was performed using the standard protocol of the Vectastain Elite ABC Universal kit (Cat No. PK-6200, Vectorlabs), as also previously reported[51]. Briefly, antigen retrieval was performed by incubating the slides in preheated citrate buffer (pH 6) in a pressure cooker for 10 min. The slides were allowed to cool at room temperature and rinsed with 1X TBST (Tris-Buffered saline with 1% Tween 20). The endogenous peroxidase activity in tissue was blocked by incubating the slides in 3% hydrogen peroxide. The slides were blocked by horse serum for 1 h before incubating with the MMP10 primary antibody (Human MMP10 monoclonal antibody, Cat No. MAB910, Bi Biotech) overnight at 4 °C in a moist chamber. Post incubation, the slides were rinsed with 1X TBST and incubated with a universal secondary antibody (Vectastain Elite ABC Universal kit). The chromogenic reaction was performed using 3,3'-diaminobenzidine chromogen solution for 5 min which resulted in brown color staining. The slides were rinsed in deionized water and counterstained with hematoxylin. Finally, the slides were dehydrated and mounted with DPX mounting medium and coverslip. Further, the immunohistochemistry staining was evaluated. Based on the IHC staining score for MMP10, +3 (strong staining) and +2 (moderate staining) scores were considered as high expression, and +1 (weak staining) and 0 (no staining) scores were considered as low expression of MMP10.

Orthotopic tongue tumor mouse model and IVIS imaging. All in vivo experiments were performed as approved by Institutional Animal Ethics Committee (IAEC), TMC-ACTREC. Luciferase-expressing stable clones of AW13516 cells stably overexpressing empty vector or *MMP10*, AW8507 and CAL27 (*MMP10* knockdown (sh-2) and vector control clones). CAL27 (1×10^6 cells), AW13516 and AW8507 (2×10^6 cells) clones were trypsinized and suspended in 40 µL sterile 1X PBS. Cells were injected orthotopically into the tongue of 6–8 week old female nude mice ($n = 6$/group) using needle gauge (30 G) after anaesthetizing the mice with isoflurane. Mice in the control group were injected with vector control cells. Caliper measurements were performed after every 7 days to monitor the volumes of the tumors using following formula: [length (mm) × (breadth)^2 (mm)^2]/2. Tumor formation was confirmed by non-invasive bioluminescence imaging (IVIS Spectrum, In Vivo Imaging System, Caliper Life Sciences) at the Molecular Imaging Facility, ACTREC. Mice were anesthetized by continuous 2% isoflurane inhalation and 100 µL of 30 mg/mL of D-luciferin substrate (D-Luciferin Firefly, potassium salt, Cat No. L-8220, Biosynth Carbosynth) was injected intraperitoneally for bioluminescence imaging (BLI). Living Image 4.5 software was used to measure bioluminescence signal peak using auto exposure mode. For the assessment of metastasis, mice were sacrificed and subjected for BLI imaging after excision of complete tongue with the primary tumor. Further, mice were dissected for ex-vivo BLI imaging of internal organs (submaxillary glands and cervical lymph nodes, lungs, liver, kidney, spleen, uterus and ovaries) collected in petri dish and sprayed with D-luciferin substrate to assess distant metastasis using IVIS system.

Survival analysis. Survival analysis was performed using Kaplan–Meier plotter online tool[52] in 499 TCGA-HNSC samples. TCGA-HNSC clinical data was directly imported into the Kaplan-Meier plotter server using the Pan-cancer RNA-seq data. *MMP10* expression status (high or low) was assigned to the samples assessed in the survival analysis based on the "Auto select cut-off" option, which selects the best performing cut-off between the upper and lower quartiles.

Statistics and reproducibility. Correlation between expression of genes and nodal status/other clinical parameters, in the in-house and TCGA-HNSC data, was performed using R programming (www.r-project.org). Statistical analysis was performed using GraphPad Prism version 8 software (GraphPad Software, La Jolla, CA). Mann–Whitney test was used to calculate the statistical significance of MMP10 expression in node positive and node negative tongue tumor samples. The student's unpaired *t*-test was used to determine the statistical significance between different groups and the *p*-values calculated are denoted as *ns* (not significant); *$p < 0.05$; **$p < 0.01$; ***$p < 0.001$; ****$p < 0.0001$. Reproducibility of the experimental findings were confirmed by performing $n = 3$ independent replicates of each experiment. The findings of all the biological replicates were consistent.

References

1. Sung, H. et al. Global cancer statistics 2020: GLOBOCAN estimates of incidence and mortality worldwide for 36 cancers in 185 countries. *CA: A Cancer J. Clinicians* **71**, 209–249 (2021).
2. Li, Y., Gupta, B. & Johnson, N. W. Systematic review and meta-analysis of association of smokeless tobacco and of betel quid without tobacco with incidence of oral cancer in south asia and the pacific. *PLoS One* **9**, e113385 (2014).
3. García-Martín, J. M. et al. *Epidemiology of Oral Cancer* (Springer Nature, 2019).
4. Yang, W. et al. Lingual lymph node metastasis in cT1-2N0 tongue squamous cell carcinoma: is it an indicator for elective neck dissection. *Front. Oncol.* https://doi.org/10.3389/fonc.2020.00471 (2020).
5. Kuroshima, T. et al. Prognostic impact of lingual lymph node metastasis in patients with squamous cell carcinoma of the tongue: a retrospective study. *Sci. Rep.* https://doi.org/10.1038/s41598-021-99925-2 (2021).
6. Larsen, S. R., Johansen, J., Sørensen, J. A. & Krogdahl, A. The prognostic significance of histological features in oral squamous cell carcinoma. *J. Oral. Pathol. Med.* **38**, 657–662 (2009).
7. D'Cruz, A. K. et al. Elective versus therapeutic neck dissection in node-negative oral cancer. *N. Engl. J. Med.* **373**, 521–529 (2015).
8. Ho, A. S. et al. Metastatic lymph node burden and survival in oral cavity cancer. *J. Clin. Oncol.* **35**, 3601–3609 (2017).
9. Stacker, S. A., Achen, M. G., Jussila, L., Baldwin, M. E. & Alitalo, K. Lymphangiogenesis and cancer metastasis. *Nat. Rev. Cancer* **2**, 573–583 (2002).
10. Biswas, N. K. et al. Lymph node metastasis in oral cancer is strongly associated with chromosomal instability and DNA repair defects. *Int. J. Cancer* **145**, 2568–2579 (2019).
11. Upadhyay, P. et al. Genomic characterization of tobacco/nut chewing HPV-negative early stage tongue tumors identify MMP10 as a candidate to predict metastases. *Oral. Oncol.* **73**, 56–64 (2017).
12. Zhang, G., Miyake, M., Lawton, A., Goodison, S. & Rosser, C. J. Matrix metalloproteinase-10 promotes tumor progression through regulation of angiogenic and apoptotic pathways in cervical tumors. *BMC Cancer* https://doi.org/10.1186/1471-2407-14-310 (2014).
13. Deraz, E. M. et al. MMP-10/Stromelysin-2 promotes invasion of head and neck cancer. *PLoS One* **6**, e25438 (2011).
14. Mariya, T. et al. Matrix metalloproteinase-10 regulates stemness of ovarian cancer stem-like cells by activation of canonical Wnt signaling and can be a target of chemotherapy-resistant ovarian cancer. *Oncotarget* **7**, 26806–26822 (2016).
15. Frederick, L. A. et al. Matrix metalloproteinase-10 is a critical effector of protein kinase Cι-Par6α-mediated lung cancer. *Oncogene* **27**, 4841–4853 (2008).
16. Regala, R. P. et al. Atypical protein kinase Cι Is required for bronchioalveolar stem cell expansion and lung tumorigenesis. *Cancer Res.* **69**, 7603–7611 (2009).
17. Algül, H. et al. Matrix metalloproteinase-10 promotes Kras-mediated bronchio-alveolar stem cell expansion and lung cancer formation. *PLoS One* **6**, e26439 (2011).
18. Kessenbrock, K., Plaks, V. & Werb, Z. Matrix Metalloproteinases: regulators of the Tumor Microenvironment. *Cell* **141**, 52–67 (2010).
19. Shi, X. et al. AJUBA promotes the migration and invasion of esophageal squamous cell carcinoma cells through upregulation of MMP10 and MMP13 expression. *Oncotarget* **7**, 36407–36418 (2016).
20. Choi, Y. J. et al. AXL and MET receptor tyrosine kinases are essential for lung cancer metastasis. *Oncol. Rep.* **37**, 2201–2208 (2017).
21. Lee, C.-H. et al. Tumor-associated macrophages promote oral cancer progression through activation of the Axl signaling pathway. *Ann. Surgical Oncol.* **21**, 1031–1037 (2013).
22. Bais, M. V., Kukuruzinska, M. & Trackman, P. C. Orthotopic non-metastatic and metastatic oral cancer mouse models. *Oral. Oncol.* **51**, 476–482 (2015).
23. Huang, X. et al. Wnt7a activates canonical Wnt signaling, promotes bladder cancer cell invasion, and is suppressed by miR-370-3p. *J. Biol. Chem.* **293**, 6693–6706 (2018).
24. Ji, J. et al. miR-944 inhibits cell migration and invasion by targeting MACC1 in nasopharyngeal carcinoma. *Int. J. Clin. Exp. Pathol.* **11**, 1167–1174 (2018).
25. Peng, H.-Y. et al. MiR-944/CISH mediated inflammation via STAT3 is involved in oral cancer malignance by cigarette smoking. *Neoplasia* **22**, 554–565 (2020).
26. Park, S. et al. microRNA-944 overexpression is a biomarker for poor prognosis of advanced cervical cancer. *BMC Cancer* https://doi.org/10.1186/s12885-019-5620-6 (2019).
27. Tang, J. et al. miR-944 suppresses EGF-induced EMT in colorectal cancer cells by directly targeting GATA6. *Onco Targets Ther.* **14**, 2311–2325 (2021).
28. Shinh, Y.-S. et al. Expression of Axl in lung adenocarcinoma and correlation with tumor progression. *Neoplasia* **7**, 1058–1064 (2005).
29. Tai, K. Y., Shieh, Y. S., Lee, C. S., Shiah, S. G. & Wu, C. W. Axl promotes cell invasion by inducing MMP-9 activity through activation of NF-κB and Brg-1. *Oncogene* **27**, 4044–4055 (2008).
30. Lee, C. H. et al. Tumor-associated macrophages promote oral cancer progression through activation of the Axl signaling pathway. *Ann. Surg. Oncol.* **21**, 1031–1037 (2014).
31. Brand, T. M. et al. AXL is a logical molecular target in head and neck squamous cell carcinoma. *Clin. Cancer Res.* **21**, 2601–2612 (2015).
32. Cardone, C. et al. AXL is a predictor of poor survival and of resistance to anti-EGFR therapy in RAS wild-type metastatic colorectal cancer. *Eur. J. Cancer* **138**, 1–10 (2020).
33. Liu, H. et al. Overexpression of matrix metalloproteinase 10 is associated with poor survival in patients with early stage of esophageal squamous cell carcinoma. *Dis. Esophagus* **25**, 656–663 (2012).
34. Campbell, M., Sticht, C., De La Torre, C., Parveen, A. & Gretz, N. miRWalk: An online resource for prediction of microRNA binding sites. *Plos One* **13**, e0206239 (2018).
35. Betel, D., Koppal, A., Agius, P., Sander, C. & Leslie, C. Comprehensive modeling of microRNA targets predicts functional non-conserved and non-canonical sites. *Genome Biol.* **11**, R90 (2010).
36. Tsang, J. S., Ebert, M. S. & van Oudenaarden, A. Genome-wide dissection of MicroRNA functions and cotargeting networks using gene set signatures. *Mol. Cell* **38**, 140–153 (2010).
37. Chen, Y. & Wang, X. miRDB: an online database for prediction of functional microRNA targets. *Nucleic Acids Res.* **48**, D127–D131 (2020).
38. Vejnar, C. E., Blum, M. & Zdobnov, E. M. miRmap web: comprehensive microRNA target prediction online. *Nucleic Acids Res.* **41**, W165–W168 (2013).
39. Hsu, S. D. et al. miRNAMap 2.0: genomic maps of microRNAs in metazoan genomes. *Nucleic Acids Res.* **36**, D165–D169 (2007).
40. Krek, A. et al. Combinatorial microRNA target predictions. *Nat. Genet.* **37**, 495–500 (2005).
41. Kertesz, M., Iovino, N., Unnerstall, U., Gaul, U. & Segal, E. The role of site accessibility in microRNA target recognition. *Nat. Genet.* **39**, 1278–1284 (2007).
42. Kruger, J. & Rehmsmeier, M. RNAhybrid: microRNA target prediction easy, fast and flexible. *Nucleic Acids Res.* **34**, W451–W454 (2006).
43. Agarwal, V., Bell, G. W., Nam, J.-W & Bartel, D. P. Predicting effective microRNA target sites in mammalian mRNAs. *eLife* https://doi.org/10.7554/eLife.05005 (2015).
44. Morgenstern, J. P. & Land, H. Advanced mammalian gene transfer: high titre retroviral vectors with multiple drug selection markers and a complementary helper-free packaging cell line. *Nucleic Acids Res.* **18**, 3587–3596 (1990).
45. Trapnell, C. et al. Differential gene and transcript expression analysis of RNA-seq experiments with TopHat and Cufflinks. *Nat. Protoc.* **7**, 562–578 (2012).
46. Tarazona, S. et al. Data quality aware analysis of differential expression in RNA-seq with NOISeq R/Bioc package. *Nucleic Acids Res.* https://doi.org/10.1093/nar/gkv711 (2015).
47. Fabregat, A. et al. Reactome pathway analysis: a high-performance in-memory approach. *BMC Bioinformatics*, https://doi.org/10.1186/s12859-017-1559-2 (2017).
48. Irizarry, R. A. Exploration, normalization, and summaries of high density oligonucleotide array probe level data. *Biostatistics* **4**, 249–264 (2003).
49. Donze, O. RNA interference in mammalian cells using siRNAs synthesized with T7 RNA polymerase. *Nucleic Acids Res.* **30**, 46e–46 (2002).
50. Boehm, J. S. et al. Integrative genomic approaches identify IKBKE as a breast cancer oncogene. *Cell* **129**, 1065–1079 (2007).
51. Upadhyay, P. et al. Notch pathway activation is essential for maintenance of stem-like cells in early tongue cancer. *Oncotarget* **7**, 50437–50449 (2016).
52. Nagy, Á., Munkácsy, G. & Győrffy, B. Pancancer survival analysis of cancer hallmark genes. *Sci. Rep.* https://doi.org/10.1038/s41598-021-84787-5 (2021).

Author contributions
B.D. and A.D. conceptualized the study and designed the experiments. B.D., A.B., A.P., S.D., P.U., A.R., R.K., S.M. and R.T. performed the experiments. B.D., A.B., A.P., S.D., A.R. and A.D. performed the data analysis. K.S., R.V., M.B., P.G., A.K.D. and S.N. generated reagents and provided clinical samples. B.D., R.K. and A.D. wrote the manuscript. All authors read and approved the final manuscript.

Competing interests
The authors declare no competing interests.

Additional information
Supplementary information The online version contains supplementary material available at https://doi.org/10.1038/s42003-023-04437-6.

Correspondence and requests for materials should be addressed to Sudhir Nair or Amit Dutt.

Peer review information *Communications Biology* thanks Yasusei Kudo and the other, anonymous, reviewers for their contribution to the peer review of this work. Primary Handling Editor: Zhijuan Qiu. Peer reviewer reports are available.

Reprints and permission information is available at http://www.nature.com/reprints

Publisher's note Springer Nature remains neutral with regard to jurisdictional claims in published maps and institutional affiliations.